



# In Situ Measurements of Melt-Pool Length and Cooling Rate During 3D Builds of the Metal AM-Bench Artifacts

Jarred C. Heigel<sup>1</sup> · Brandon M. Lane<sup>2</sup> · Lyle E. Levine<sup>2</sup>

Received: 6 November 2019 / Accepted: 22 January 2020 / Published online: 20 February 2020

© This is a U.S. government work and its text is not subject to copyright protection in the United States; however, its text may be subject to foreign copyright protection 2020

## Abstract

This work provides results and analysis of the in situ thermal measurement acquired during the 3D builds performed for the 2018 additive manufacturing benchmark tests. The objective is to provide context for post-process characterization of distortion, residual strain, and microstructure, which are reported elsewhere in this Journal, and to provide validation data for thermal models of the build process. Four bridge artifacts (75 mm long, 5 mm wide, 12.5 mm tall) are created in each of three builds using a commercial laser powder bed fusion system. The builds are performed using nickel super alloy 625 (IN625). High-speed infrared thermography performed during four of the builds is used to measure the melt-pool length and cooling rate within a select region. The temperature of the substrate and build volume is measured during the fifth build to provide data to establish the boundary conditions for thermal models.

**Keywords** Additive manufacturing · Model validation · 3D build · Inconel 625 · Temperature measurement · Cooling rate

## Introduction

The outcome of metal-based additive manufacturing (AM) is dependent on the temperature history experienced throughout the part during the manufacturing process. High-intensity energy sources, either lasers or electron beams, are used to melt feedstock layer by layer to create the part. As the molten feedstock material solidifies, not only is the part created, but also is the microstructure, which is sensitive to the cooling rate of the material. Unfortunately, the newly solidified material experiences frequent and rapid heating cycles

as additional feedstock material is melted and added to the part, resulting in a complex thermal history that generates residual stress and distortion in the part and produces a final material state that is challenging to predict.

Existing research has demonstrated the effect of process conditions, which generate the temperature history, on the final part quality. Deleterious residual stress/strain is generated by the intense thermal cycling experienced in parts manufactured using AM. This impact was demonstrated by Denlinger and Michaleris [1] who showed that distortion on the magnitude of 10 mm was generated in a large Ti–6Al–4V part manufactured using a wire-fed electron-beam directed energy deposition (DED) process. The distortion was then minimized through process optimization using a thermo-mechanical model that was validated by measuring in situ distortion and temperature (using thermocouples) of a cantilevered test substrate [2]. Process models for laser powder bed fusion (LPBF) have similarly been developed and validated using distortion and temperature measurements of the substrate [3]. Other works have demonstrated the sensitivity of stress/strain and distortion to processing conditions. For instance, the residual stress/strain and distortion of metal arches fabricated using different scan strategies were measured and compared, demonstrating the sensitivity to scan strategy [4, 5]. However, the objective of these works

---

This document is an official contribution of the National Institute of Standards and Technology (NIST), not subject to copyright in the USA. The full descriptions of the procedures used in this paper require the identification of certain commercial products. The inclusion of such information should in no way be construed as indicating that such products are endorsed by NIST or are recommended by NIST or that they are necessarily the best materials, instruments, software, or suppliers for the purposes described.

---

✉ Jarred C. Heigel  
jarred.heigel@thirdwavesys.com

<sup>1</sup> Third Wave Systems, Eden Prairie, MN 55344, USA

<sup>2</sup> National Institute of Standards and Technology, Gaithersburg, MD 20899, USA

was stress/strain and distortion of the bulk part, therefore providing limited insight into the material state generated near the melt-pool.

Other researchers have focused on the microstructure generated by AM processes. The solidification of the melt-pool during AM processes is fundamentally similar to the welding process, which is summarized by David and Vitek [6]. However, the large scale of AM processes that fabricate complex geometries using thousands of scan-tracks (weld beads) complicates the analysis. For instance, Antonysamy and colleagues demonstrated the impact of part geometry on grains developed during electron beam powder bed fusion (E-beam PBF) of Ti–6Al–4V [7]. Their work demonstrated grain sizes varying significantly in correlation to the scan strategy and location within the part. The authors note from a comparison of electron backscatter diffraction (EBSD) analysis at different layers within a part that the grain texture varies with build height. Based on these results, the authors theorize that melt-pool solidification conditions that result in the different texture are marginal, but unfortunately, the change in solidification conditions was not understood. Others have manipulated the melt-pool solidification conditions using scan strategy to create different microstructures. For example, Dehoff and colleagues demonstrated their ability to use E-beam processing parameters to control grain size [8]. Their demonstration involved creating the Department of Energy acronym (DOE) with fine grains within a bulk structure comprised of larger grains. Although these studies have drawn conclusions based on simulation results, basic temperature measurements, or inferences based on theory, none of these studies have implemented direct measurement of the temperatures around the melt-pool to better understand the thermal history responsible for the resulting microstructure.

Thermography enables measurement of the thermal behavior on the surface and surrounding area of the melt-pool that can be used to understand the material development. Kriczky et al. [9] implemented coaxial thermography to measure the melt-pool dimensions and thermal gradient in the entirety of a L-shaped specimen. This work demonstrated a sensitivity to build height and wall thickness that could impact the final material state. Carroll et al. [10] performed a similar thin-walled build at the same institution to study the mechanical properties. Results showed a sensitivity to build height and attributed this to the changing temperature history as a function of build height. Bennett et al. [11] used an infrared (IR) camera to measure the temperature during the fabrication of a thin wall of IN 718. After testing micro-tensile bars extracted from locations within the wall, the results were correlated with the temperature history experienced by each test specimen. Despite the potential impact of these studies on building the correlation between temperature history and material state, extrapolating these results to PBF processes may be challenging due to the

smaller spatial and faster temporal scales in PBF processes, which create significantly higher cooling rates, steeper temperature gradients, and shorter solidification times.

Several researchers have performed thermography during PBF processes cameras in a staring configuration, which observe a fixed region on the build plane. Krauss et al. [12] used a long-wave IR camera with a 50 Hz frame rate to measure the thermal history and to demonstrate the ability to detect artificial flaws from deviations in the cooling rate. Craeghs et al. [13] utilized a thermal camera to detect thermal variations when building components over supports structures. Recently, the variability of cooling rate was quantified in a small part with bulk, thin-wall, and overhang features [14]. These results show significant variability within the build section due to the scan strategy, and that the thin walls increase the cooling rate, while the overhang decreases the cooling rate. Hooper [15] correlated processing parameters and part features with melt-pool dynamics and temperature gradients by implementing coaxial multi-wavelength high-speed cameras. Unfortunately, no correlation was made between the thermal histories measured in these studies and the resulting microstructure or residual stress/strain.

Some work has been performed correlating material state with thermal processing conditions in PBF processes. Lane et al. [16] used an IR camera system with a fast frame rate (1800 Hz) to measure the thermal history in a part with a 45° overhang. Thermal measurements revealed a chaotic behavior due to spatter and retained heat near the edge of the overhang. The microstructure from this experiment was studied by Arisoy et al. [17], who correlated the grain size and growth orientation with the scan strategy. However, no residual stress/strain measurements were performed.

It is difficult to directly link data between studies because of the process differences between DED, LPBF, and E-beam PBF; the difference between machines arising from intellectual property and patents of the manufacturers; the lack of standards or best practices for build and process development; and the nearly limitless build strategy variations such as power, speed, scan orientation, etc. Therefore, to develop the relationships between temperature history, microstructure, and residual stress/strain, and to provide data for model validation, rigorous experiments are required to correlate these phenomena and provide the necessary model validation data.

The objective of this paper is to provide measurements and analysis of the temperatures experienced during the 2018 AM-Bench metal 3D builds. Each build creates a bridge structure with legs of three different sizes. In situ measurements are performed using high-speed thermography and thermocouples welded to the substrate and build volume. Melt-pool length and cooling rate are calculated from the thermography measurements. The results are used to investigate the effect of scan strategy and geometry

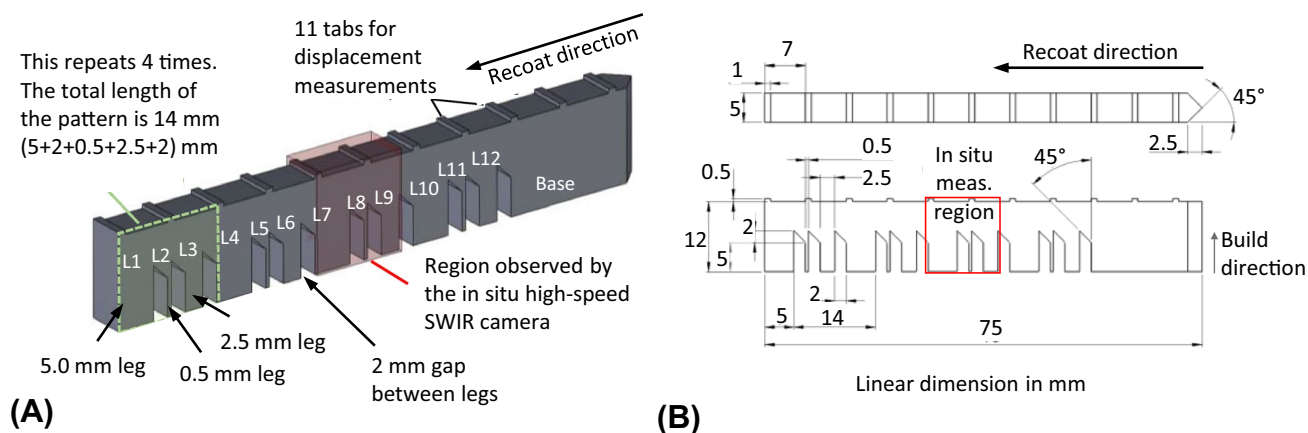


**Fig. 1** The bridge structure geometry used in this study and for AM-Bench challenge AMB2018-01

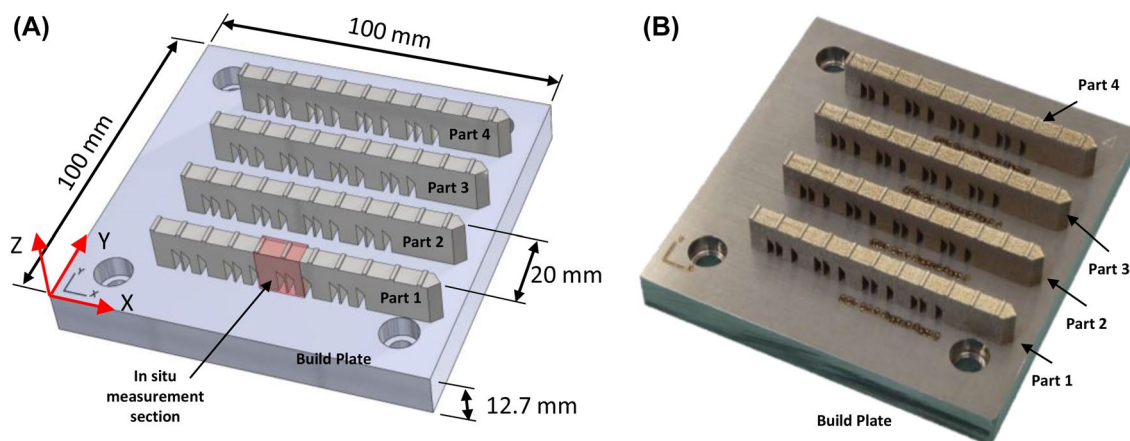


**Fig. 2** Build layout of the four bridge structures on the 100-mm square substrate. **a** A diagram of the layout with the in situ measurement region highlighted, **b** a photograph of a completed build

on thermal history and for comparison to the single-track measurements reported by Lane et al. [18]. The analysis also provides context for the stress and microstructure analysis performed on these artifacts and reported elsewhere in this journal issue. Residual strain and the resulting distortion are measured [19]. Three different methods were used to measure and map the residual strain of the part: neutron diffraction, synchrotron X-ray diffraction, and the contour method. The distortion resulting from partial separation of the part from the substrate is measured using a coordinate measuring machine (CMM). Select legs are cross-sectioned to measure the location-specific microstructure [20] and phase evolution [21]. Since cross sections from only select legs of the part are analyzed, the cooling rate analysis presented herein is used to explore the possibility of using these legs as proxies for the other features that are not cross-sectioned.

## Methodology

The experiments were performed using a commercial LPBF machine to manufacture 3D metal alloy bridge structures while measuring the temperature in situ. The bridge structure, shown in Fig. 1, is 12.5 mm tall, 75.0 mm long, and 5 mm wide. The bottom half of the geometry consists of twelve 5.0-mm-tall legs of varying size and a larger base. The twelve legs consist of four sets of three different sizes: the largest legs (L1, L4, L7, and L10) measure 5.0 mm × 5.0 mm, the medium sized legs (L3, L6, L9, and L12) measure 2.5 mm × 5.0 mm, and the smallest legs (L2, L5, L8, and L11) measure 0.5 mm × 5.0 mm. A subset of the largest and smallest legs is cross-sectioned and analyzed by Phan et al. [19] and Stoudt et al. [20]. Each of the legs is separated by a 2.0-mm gap. A high-speed InSb thermal camera, which is filtered to short-wave infrared (SWIR)

**Table 1** Summary of the builds and in situ measurements performed for the 2018 AM-Bench

AM-Bench build name	Material	Build date	Build time	Measurements
AMB2018-01-625-Build1	IN625	2018, January 30	9 h 23 min	Melt-pool length, cooling rate
AMB2018-01-625-Build2	IN625	2018, February 1	9 h 22 min	Melt-pool length, cooling rate
AMB2018-01-625-Build3 <sup>a</sup>	IN625	2018, December 19	9 h 6 min	Substrate/build volume temperature

<sup>a</sup>Build time is shorter than other builds. The machine was serviced, and laser was replaced between 625-Build2 and 625-Build3

(1350–1600 nm), was used to measure the temperature history of every layer within a small section of the part that contains one example of each of the three different leg geometries.

The top half of the geometry consists of a single 5-mm-tall bridge section that connects the legs to the base. Overhangs that are 45° and 2 mm tall transition the legs and base into the bridge section. Eleven 0.5-mm-tall tabs are fabricated on the top of the bridge to facilitate post-process distortion measurements detailed in [19].

## Build Description

Four parts are fabricated on 100 mm square, 12.7-mm-thick substrates, as shown in Fig. 2. The substrates are bolted to the center of the 250-mm square steel build surface in the LPBF machine. The parts are spaced by 20 mm along the *Y* axis of the substrate, and they are offset from each other along the *X* axis by 0.5 mm so that the recoating blade progressively engages each part. The parts are fabricated in the order they are labeled (Part 1 first and Part 4 last). Multiple builds are performed, as shown in Table 1, using virgin nickel super alloy 625 (IN625) powders. The substrate material in each build is IN625. “Build Parameters and Scan Strategy” section briefly describes the build process. Greater detail on the build description and characterization of the powder is found in [22]. Videos describing the builds processes are available through the AM-Bench website.<sup>1</sup>

Table 1 outlines the in situ measurements performed during each build. A high-speed in situ thermography system is used to measure melt-pool lengths and cooling rates during two of the builds. Each of these two builds was executed using identical build strategies and process parameters, with the only difference being the virgin powder and substrate material.

A third IN625 build was executed on December 19, 2018, to measure the substrate and build volume temperatures. The methodology and results are reported in “Appendix” section. The decision to perform these measurements was based on feedback received after the 2018 AM-Bench conference. This feedback indicated that the modeling community will

use these measurements to define the thermal boundary conditions and improve the accuracy of the thermal models of the process.

This third build is intended to replicate the prior builds. This build used virgin IN625 powder from the same lot as the earlier IN625 builds. Despite using the same build file as the previous builds, the total build time was approximately 16 min shorter. Although the cause of the difference in build duration is unknown, possible causes are changes to the machine and/or software resulting from the maintenance performed by the manufacturer during the summer of 2018. During this service, the laser was also replaced and calibrated by the manufacturer.

## Build Parameters and Scan Strategy

Figure 3 illustrates the build process. Each layer of the build proceeds by first scanning the contours and then using an infill scan to solidify the material within the contours. The infill scans are executed with a programmed laser power of 195 W and scan speed of 800 mm/s. According to the manufacturer, the  $D4\sigma$  laser diameter on the build plane is 85  $\mu\text{m}$  during the contour scans, but defocuses to 100  $\mu\text{m}$  for the infill scans. The distance between adjacent scan lines (hatch distance) is 0.1 mm. The infill scan pattern is parallel to the *X* axis during odd-numbered layers and parallel to the *Y* axis during even-numbered layers. The build platform is lowered 0.02 mm between each layer to spread a new layer of virgin powder across the powder bed. The time between the completion of the last infill scan line on a part and the beginning of the first contour of the next part ranges from 0.307 to 0.363 s. This time variation is a function of where the last infill scan concludes and where the first contour scan begins.

During the fabrication of the legs during Layers 1 through 250 ( $Z = 0.02$  mm to  $Z = 5.00$  mm), an average of 52 s pass between the start of the first contour of layer  $n$  and the start of the first contour of layer  $n + 1$ . It only requires approximately 26 s to scan all four parts; however, a dwell is imposed before recoating to enable the Additive Manufacturing Metrology Testbed (AMMT)<sup>2</sup> to replicate the build

<sup>1</sup> <https://www.nist.gov/ambench/amb2018-01-description>.

<sup>2</sup> <https://www.nist.gov/el/ammt-temps>.

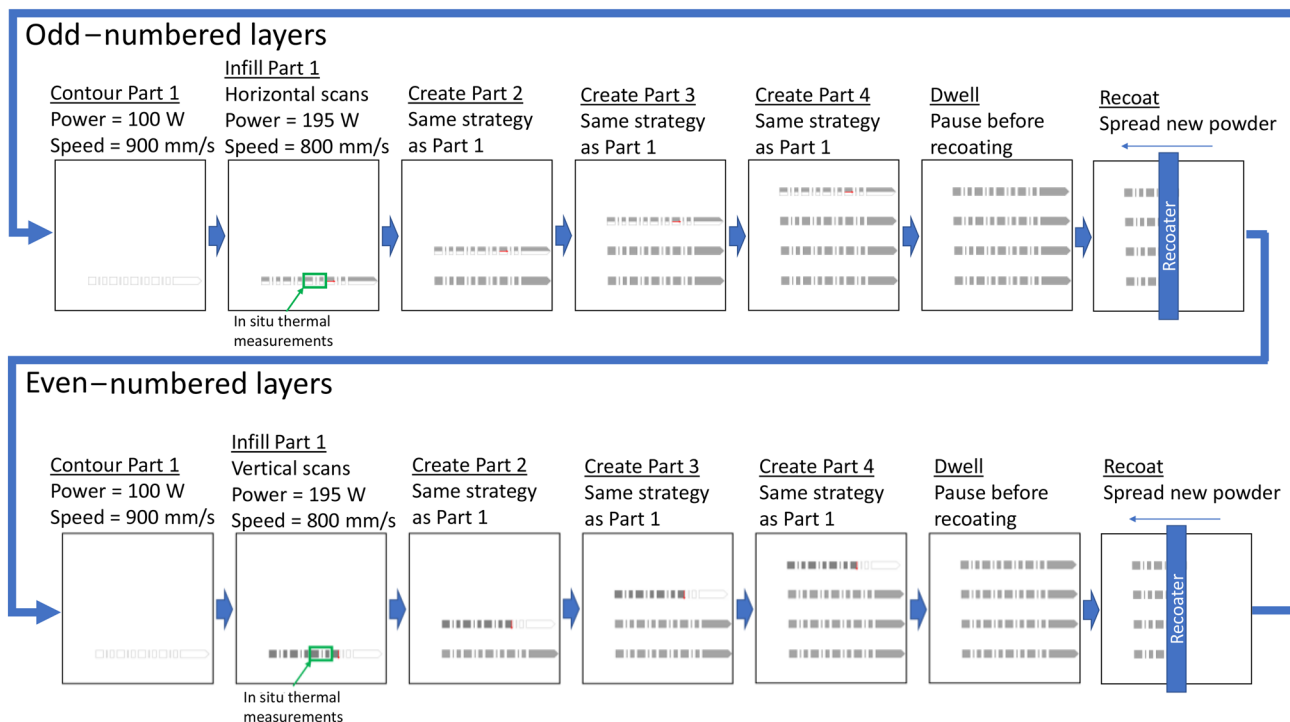


Fig. 3 Illustration of the build process

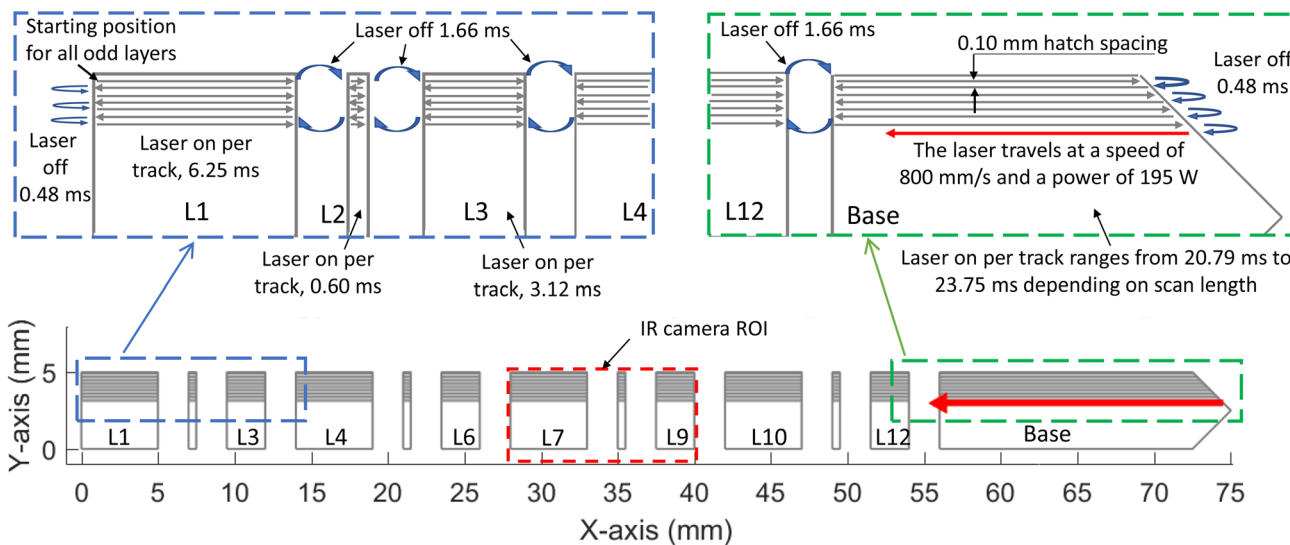
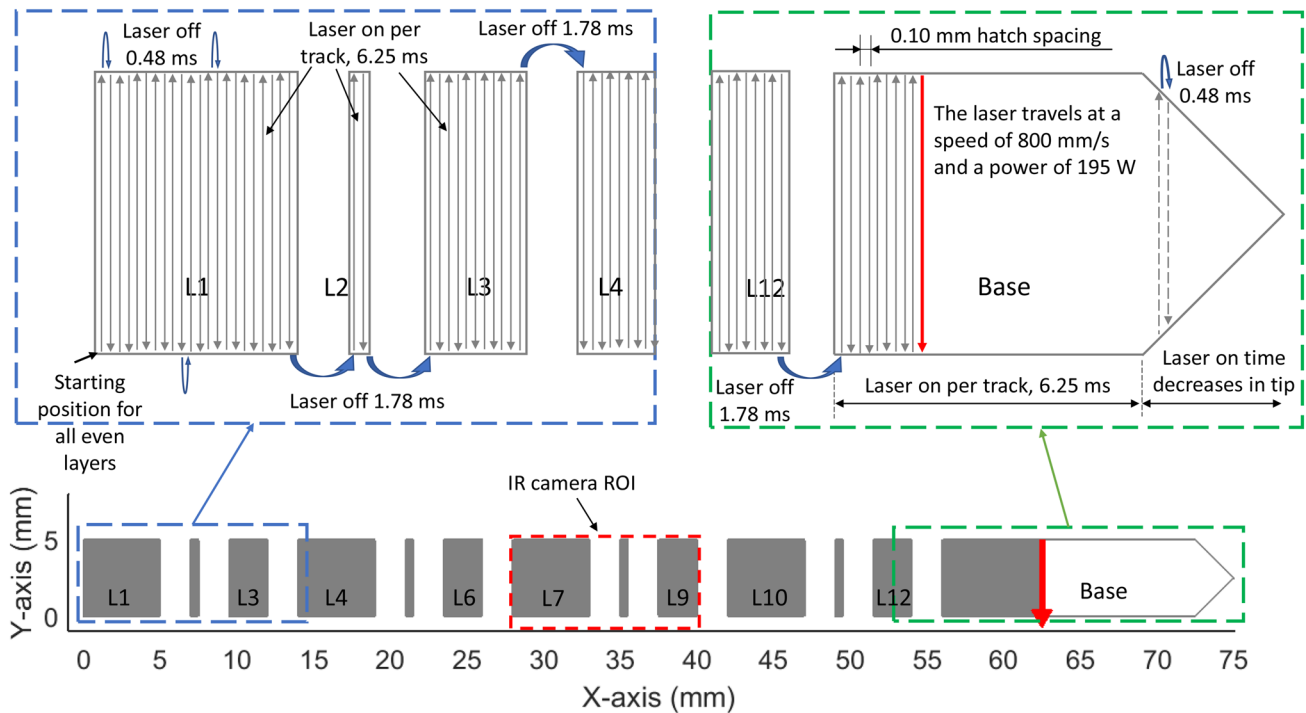


Fig. 4 Illustration of the scan strategy used for odd-numbered layers. The scale and number of scan lines in each feature depicted in the sub-figures are not accurate. The axes represent the part coordinates

in future studies. This is necessary because the AMMT has a longer duration recoating process. A high-strength steel recoating blade is used in all experiments. It spreads the new powder layer at a speed of 80 mm/s.

### Odd-Numbered Layers

Figure 4 illustrates the scan strategy and timing for the odd-numbered layers. The laser scans back-and-forth



**Fig. 5** Illustration of the scan strategy used for the even-numbered layers. The scale and number of scan lines in each feature depicted in the sub-figures are not accurate. The axes represent the part coordinates

parallel to the machine  $X$  axis. The first infill scan line of each off layer begins at the upper left corner of the part, L1, and travels to the right ( $+X$ ). The time between the laser turning off at the completion of one leg and the beginning of the next is  $(1.66 \pm 0.01)$  ms. When the laser reaches the end of the furthest feature to the right (the Base), the time between the completion of the scan line and the beginning of the next line directly below and scanning in the opposite direction is  $(0.48 \pm 0.01)$  ms. The beginning and end of each scan-track are offset 0.03 mm from the left and right edges of each feature. The durations the laser is on and off are calculated from measurements of the laser command signal obtained using an oscilloscope. These measurements were performed for Layer 3 during a trial build and are assumed to be the same for all odd-numbered layers from 1 to 250. Measurements of the overhang, bridge, and tab portions of the builds were not acquired. The laser-off times of  $(0.48 \pm 0.01)$  ms at the left and right sides are assumed to be consistent in all layers of the build.

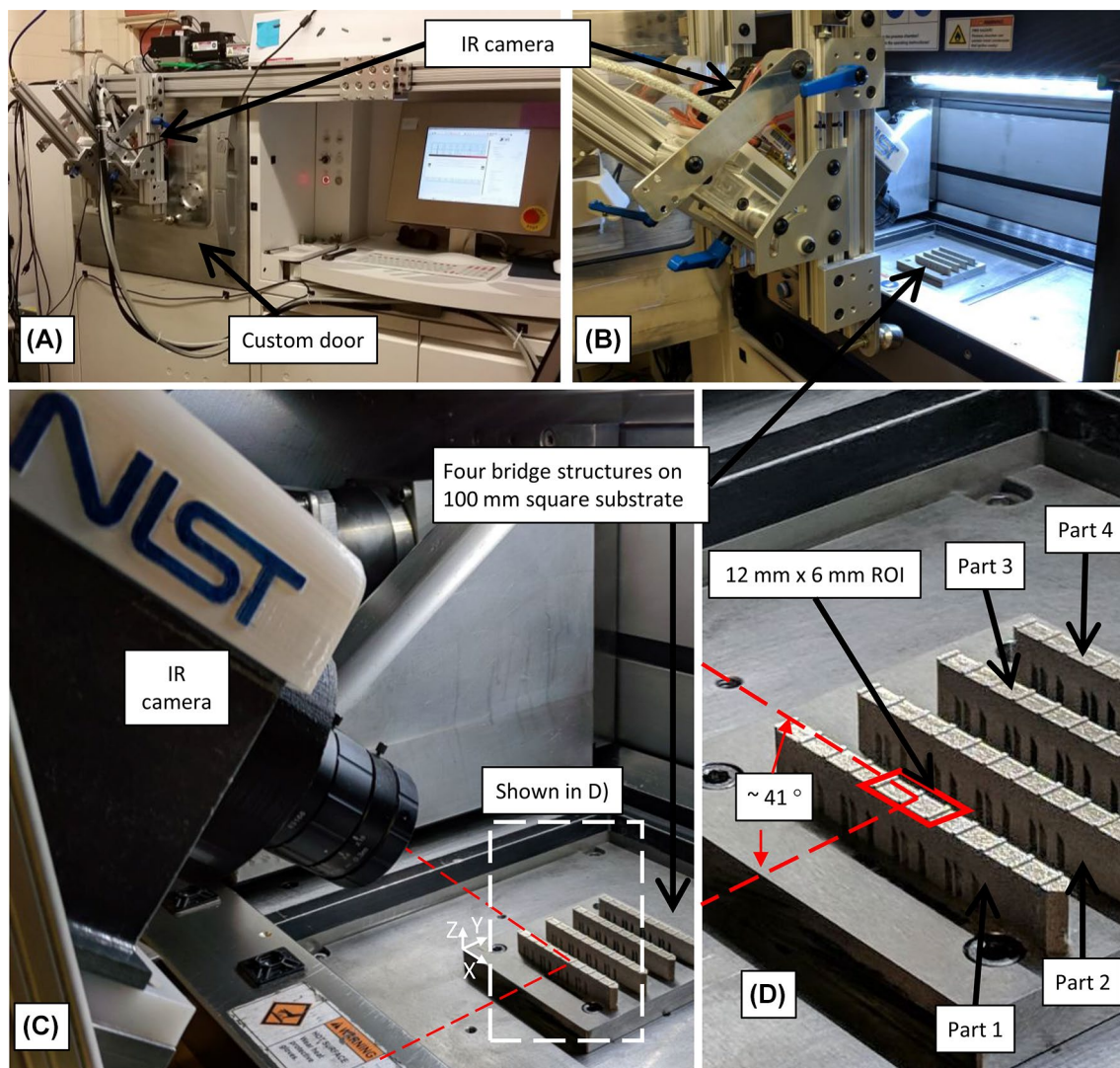
### Even-Numbered Layers

Figure 5 depicts the scan strategy for the even-numbered layers. The laser scans back-and-forth parallel to the machine  $Y$  axis. The first infill scan line begins at the lower left corner of the part in L1 and scans in the  $+Y$  direction. In contrast

to the odd-numbered layers, the infill of a feature is completed before beginning the infill of the next feature to the right. The direction of each scan alternates regardless of whether the laser is continuing to scan a single feature or is transitioning between features. The scan lines begin and end 0.03 mm from the bottom and top edges of the feature. Excluding the right edge of the base that forms the point, the durations and timing of the scan-tracks within individual features are consistent:  $(6.25 \pm 0.01)$  ms to scan a track and  $(0.48 \pm 0.01)$  ms to reposition for the next adjacent track scanning in the opposite direction. The duration the laser is off when repositioning between features is  $(1.78 \pm 0.01)$  ms. This information is determined from measurements of the laser command signal during Layer 4 of a trial build. The laser repositioning time between the overhangs is unknown.

### In Situ Infrared Temperature Measurement

Figure 6 presents the experiment setup. A custom fabricated door is mounted to the EOSint M270D [16, 23]. The custom door allows an IR camera to be positioned as close to the build as possible without obstructing the recoating arm. The close proximity allows the highest magnification using the given optical system. The camera is mounted to an articulating frame attached to the exterior of the machine. When in position for an experiment, the working distance from the lens to the object is approximately



**Fig. 6** The thermography setup. **a** The EOSint M270D LPBF system with custom door and IR camera. **b** View of the build chamber with the door open and the camera in position. A completed build is

mounted to the steel build plate for illustration. **c** Relative position of the camera to the build. **d** Magnified image of the build with four parts and the in situ ROI highlighted

162 mm, and the camera is angled approximately  $41^\circ$  from the build plane.

An IRCamera model IRC 912 is used. A band-pass filter is installed to limit the measurable wavelengths to a range from 1350 to 1600 nm. The integration time (shutter speed) of the camera is  $40 \mu\text{s}$ , and the frame rate is 1800 frames per second. The window size is limited to 360 horizontal pixels and 126 vertical pixels. Considering the camera magnification of approximately  $0.33\times$ , the working distance, and the relative angle between the camera and the target, the pixel instantaneous field of view (iFOV) in the horizontal and vertical axes is approximately  $34 \mu\text{m}$  and  $52 \mu\text{m}$ , respectively. The ratio between spatial

resolution and laser spot diameter would create significant uncertainty when attempting to calculate melt-pool width. Therefore, the calculation is not attempted. However, melt-pool length and cooling rate calculations are made, as described in “[Melt-Pool Length and Cooling Rate Calculation Methodology](#)” section.

The measured camera signal is related to the temperature of the object according to [24]:

$$S_{\text{meas}} = \epsilon F(T_{\text{true}}) = F(T_{\text{rad}}) \quad (1)$$

where  $S_{\text{meas}}$  is the camera signal in digital levels (DL),  $T_{\text{True}}$  is the black-body temperature in K,  $T_{\text{rad}}$  is the radiant

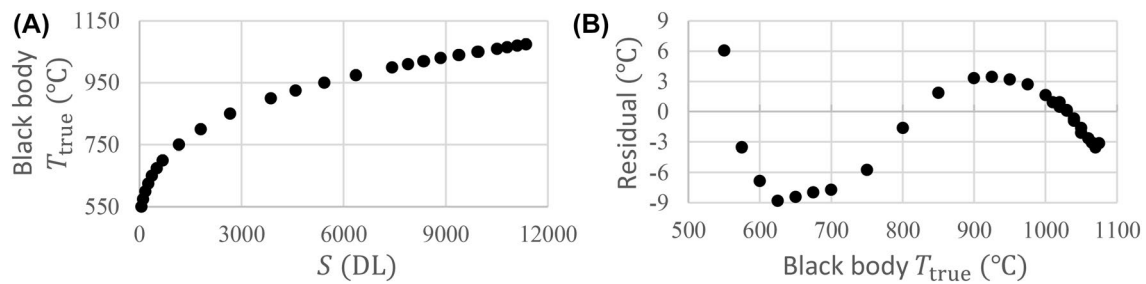


**Fig. 7** The black-body calibration and the residuals of the fit of Eq. 2 to the calibration data

temperature in K, and  $\varepsilon$  is the effective emissivity of the object. Effective emissivity is a dimensionless value between 0 and 1. Only for perfectly emitting black bodies does  $\varepsilon = 1$ ; all other bodies emit a fraction of the radiation. Consequently, the camera measures a signal in response to this radiated temperature,  $T_{\text{rad}}$  in K, and the true temperature of the object can be calculated only if  $\varepsilon$  is known. The function relating  $T_{\text{rad}}$  and  $T_{\text{true}}$  to  $S$  is defined by the Sakuma–Hattori equation and its inverse:

$$F(T_{\text{rad}}) = S = \frac{C}{\exp\left(\frac{c_2}{AT_{\text{rad}}+B}\right) - 1} \quad (2)$$

$$F^{-1}(S) = T_{\text{rad}} = \frac{c_2}{A \ln\left(\frac{C}{S} + 1\right)} - \frac{B}{A} \quad (3)$$

$$F^{-1}(S/\varepsilon) = T_{\text{true}} = \frac{c_2}{A \ln\left(\frac{C}{S/\varepsilon} + 1\right)} - \frac{B}{A} \quad (4)$$

where  $c_2$  is the second radiation constant (14 388  $\mu\text{m}/\text{K}$ ) and the coefficients  $A$ ,  $B$ , and  $C$  are determined via the black-body calibration procedure outlined by Lane and Whitenton [24]. A black body is first used to create a 2-point non-uniformity correction (NUC), and then a series of measurements are performed using the black-body that is incrementally set to temperatures covering the detectable range of the camera (550 °C to nearly 1100 °C). This range is a function of the camera settings and optical system. Figure 7 presents the results of this calibration, where  $T_{\text{BB}}$  is plotted against the average camera signal over 100 frames. The coefficients  $A = 2.665$ ,  $B = -800.7$ , and  $C = 1.94E6$  are determined by assuming  $\varepsilon = 1$  and fitting Eq. 2 to the data presented in Fig. 7a. The residuals of this fit are presented in Fig. 7b, while the root mean square error (RMSE) of the fit is 8.1 °C. The RMSE is an estimate of the calibration uncertainty,  $u_{\text{cal}}$ .

Measured radiant temperature uncertainty,  $u_{T_{\text{rad}}}$ , is defined by Eq. 5, while the true temperature uncertainty,  $u_{T_{\text{true}}}$ , is defined by Eq. 6:

$$u_{T_{\text{rad}}}^2 = \left(\frac{\partial F^{-1}(S)}{\partial S}\right)^2 u_S^2 + u_{\text{cal}}^2 + u_{\text{system}}^2 \quad (5)$$

$$u_{T_{\text{true}}}^2 = \left(\frac{\partial F^{-1}(S/\varepsilon)}{\partial \varepsilon}\right)^2 u_{\varepsilon}^2 + \left(\frac{\partial F^{-1}(S/\varepsilon)}{\partial S}\right)^2 u_S^2 + u_{\text{cal}}^2 + u_{\text{system}}^2 \quad (6)$$

In these equations,  $u_{\text{cal}}$  is the calibration uncertainty (RMSE of the fit, as described earlier), while  $u_{\text{system}}$  is a compilation of systematic measurement uncertainties, such as motion blur, optical blur, and reflections. In this work, the effect from reflections is negligible due to the wavelengths used and the high temperature of the melt-pool relative to the surroundings. At this time,  $u_{\text{system}}$  is assumed to be sufficiently small compared to the other components and is assumed to be negligible; however, the actual value of these sources of uncertainty must be determined. The uncertainty of the camera signal,  $u_S$ , is the root sum square of the effect of digitization (1 digital level) and the noise in the signal. These effects have a diminishing impact at higher camera signals (temperature). Considering that the melt-pool length and cooling rate measurements are performed at the higher range of camera signal, these effects are very small compared to the other sources of uncertainty. The emissivity uncertainty,  $u_{\varepsilon}$ , is the largest contributing factor to the temperature uncertainty and will be discussed shortly. The final parts of Eqs. 5 and 6 are the partial derivative of the inverse Sakuma–Hattori equation (Eq. 4) with respect to camera signal and emissivity:

$$\frac{\partial F^{-1}(S)}{\partial S} = \frac{c_2 C}{AS(C+S) \ln^2\left(\frac{C}{S} + 1\right)} \quad (7)$$

$$\frac{\partial F^{-1}(S/\varepsilon)}{\partial S} = \frac{c_2 C \varepsilon}{AS(C\varepsilon + S) \ln^2\left(\frac{C\varepsilon}{S} + 1\right)} \quad (8)$$



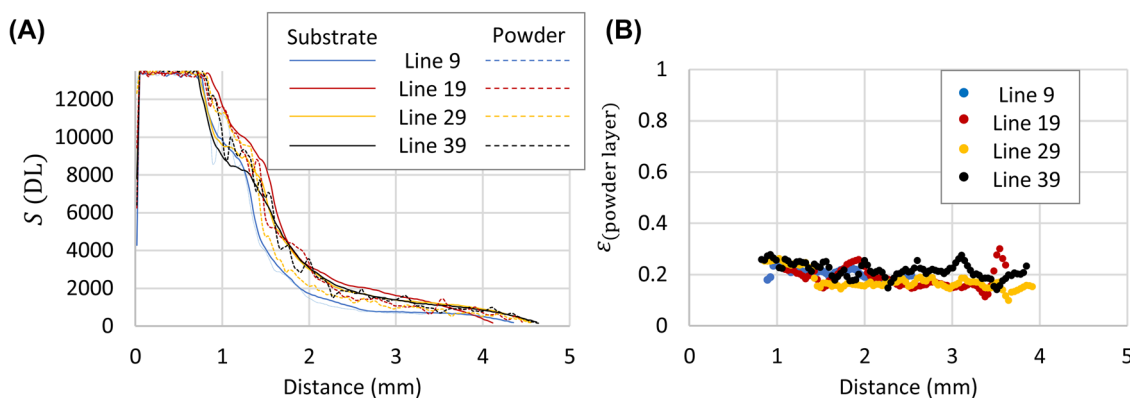


**Fig. 8** a Comparison of multi-line scan-tracks created on a bare substrate and a single layer of powder, as first reported by Heigel et al. [25]. b The ratio between the emissivity of powder layer and bare substrate, as calculated using Eq. 13

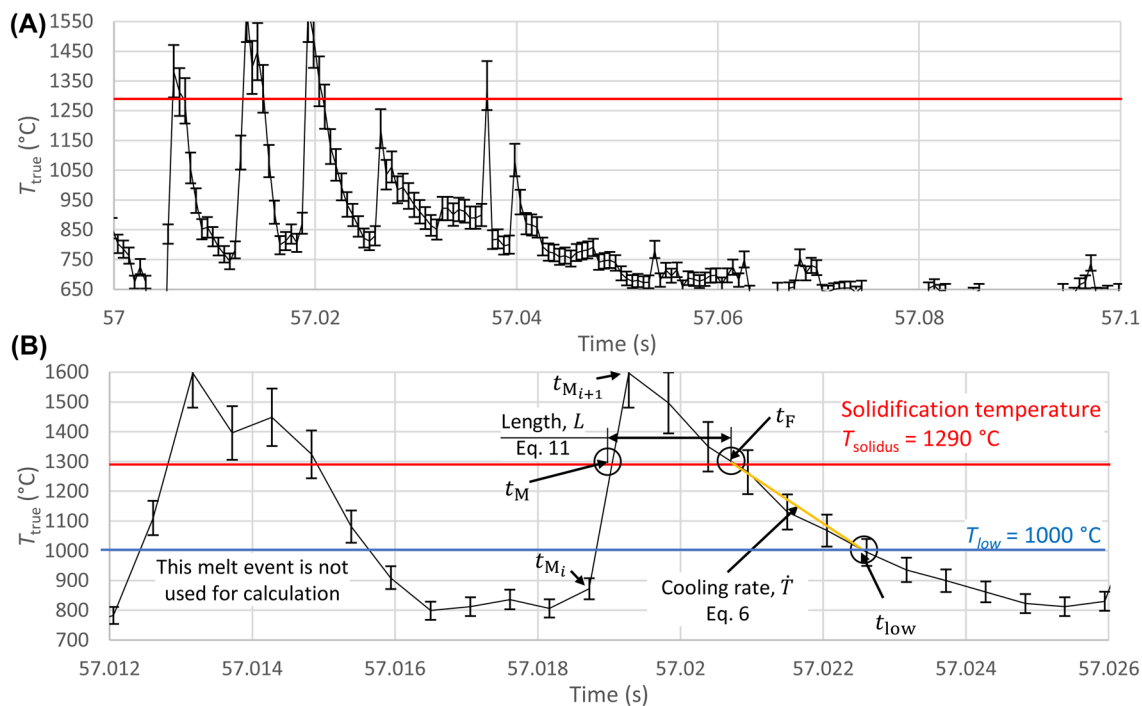


**Fig. 9** The method to measure melt-pool length and cooling rate. a The radiant temperature measured at a single pixel in the middle of L7. b Illustration of the melt-pool length and cooling rate calculation.

Error bars represent the true temperature measurement uncertainty,  $u_{T_{\text{true}}}$ , with a coverage of  $1\sigma$

$$\frac{\partial F^{-1}(S/\epsilon)}{\partial \epsilon} = \frac{c_2 C}{A(C\epsilon + S) \ln^2 \left( \frac{C\epsilon}{S} + 1 \right)} \quad (9)$$

Emissivity is equal to the empirically determine value at the solidification event, which is  $\epsilon_{\text{solidus}} = 0.221$ . This value was determined by Lane et al. [18] for this LPBF system and processing parameter combination while creating single scan-tracks on bare substrates. Prior work

by Heigel et al. demonstrated that while the inclusion of powder in single and multi-track scans increased the measured radiant temperature variability, it did not significantly affect the average of the measured value [25]. Therefore, the emissivity value determined by Lane et al. is appropriate.

Emissivity uncertainty,  $u_\epsilon$ , is determined from the measurements made by Heigel et al. and presented in Fig. 8a. In this figure, the camera signals measured during

select tracks from multi-line scans on a bare substrate and a single powder layers are compared. The emissivity of the powder-layer case,  $\epsilon_{(\text{powder layer})}$ , is calculated using the following equation and the results are presented in Fig. 8b

$$\epsilon_{(\text{powder layer})} = \frac{S_{(\text{powder layer})}}{F \left( F^{-1} \left( \frac{S_{(\text{bare substrate})}}{\epsilon_{(\text{bare substrate})}} \right) \right)} \quad (10)$$

This equation is derived from Eq. 1. The variables  $S_{(\text{bare substrate})}$  and  $S_{(\text{powder layer})}$  are the measured camera signals acquired from the bare-substrate and powder-layer scans, respectively. The variable  $\epsilon_{(\text{bare substrate})}$  is the emissivity of the bare-substrate case and is equal to the value of  $\epsilon_{\text{solidus}} = 0.221$  found by Lane et al. [18]. This allows the emissivity uncertainty to be determined by calculating the standard deviation of  $\epsilon_{(\text{powder layer})}$ , resulting in  $u_{\epsilon} = 0.0364$ .

### Melt-Pool Length and Cooling Rate Calculation Methodology

Melt-pool length and cooling rate are calculated for every pixel in each layer of the build using the strategy depicted in Fig. 9, which shows the temperature history measured by an individual pixel. No smoothing or filtering is applied. The error bars represent the radiant temperature measurement uncertainty,  $u_{T_{\text{rad}}}$ . Figure 9a demonstrates that the radiant temperature rises and falls as the laser serpentine toward and then away from the material observed by the pixel. Frequent temperature spikes occur due to melting, re-melting, and reheating caused by the laser during successive passes, and due to spatter particles flying through the pixel's field of view. Melt occurrences are determined by radiant temperature excursions above a threshold of 964 °C. Since material can be melted multiple times by adjacent scan-tracks, only the last melt occurrence is used to calculate the melt-pool length and cooling rate based on the assumption that when the material is re-melted, the microstructure and residual stress/strain created by the preceding melt event are eliminated. To avoid the possible erroneous determination of spatter as a melt occurrence, which occurs in the example in Fig. 9a at a time of 58.347 s, the final melt event is identified by the last occurrence of at least two consecutive temperature measurements above the threshold.

Melt-pool length,  $L$  (mm), is calculated using a temporal approach, where the values for individual pixels are calculated according to the temperature history of the pixel:

$$L = v(t_F - t_M) \quad (11)$$

where  $v$  is the programmed travel speed of the laser, in mm/s, and  $t_M$  and  $t_F$  are the times, in s, that the pixel temperature

crosses above (melts) and below (solidifies) the solidification temperature,  $T_{\text{solidus}}$ , respectively. The time values,  $t_M$  and  $t_F$ , are determined using linear interpolation. Melt-pool length uncertainty,  $u_L$ , is:

$$u_L^2 = \left( \frac{\partial L}{\partial v} \right)^2 u_v^2 + \left( \frac{\partial L}{\partial t_M} \right)^2 u_{t_M}^2 + \left( \frac{\partial L}{\partial t_F} \right)^2 u_{t_F}^2 \quad (12)$$

$$u_L^2 = (t_F - t_M)^2 u_v^2 + v^2 (u_{t_M}^2 + u_{t_F}^2)$$

In these equations,  $u_v$  is the scan velocity uncertainty and  $u_{t_M}$  and  $u_{t_F}$  are the uncertainties of  $t_M$  and  $t_F$ . Currently, no information exists regarding the scan speed error, but  $u_v$  is assumed to equal 0 because it is negligibly small compared to the temperature-based sources of uncertainty. However, work is required to characterize the scan motion and speed errors of these systems to establish the actual value of  $u_v$ . This will be especially important as the process temperature metrology methods improve and the associated errors are decreased. The value of  $u_{\Delta t}$  is based on the error in the timing of the acquisition of the camera frames. It is too negligibly small compared to the temperature-based sources of uncertainty and is assumed to equal 0.

The calculation of  $u_{t_M}$  is based on the acquisition timing of the frames bracketing the melt event,  $t_{M_i}$  and  $t_{M_{i+1}}$ :

$$u_{t_M} = (t_{M_{i+1}} - t_{M_i}) / \sqrt{12} \quad (13)$$

Nominally,  $t_{M_{i+1}} - t_{M_i}$  is the inverse of camera frame rate; however, frames are occasionally skipped during acquisition and a longer time than expected occurs between frames. This formulation of uncertainty is implemented because the incredibly fast heating rate from temperatures often below the measurable range of the camera to a temperature well above saturation means that the melt event has an equal probability of occurring anytime between the two frames [29]. In contrast, the relatively slower cooling rate at the back of the melt-pool allows  $u_{t_F}$  to be calculated using the slope of the temperature change (cooling rate  $\dot{T}$ ) and uncertainty in the solidus temperature  $u_{T_{\text{solidus}}}$ :

$$u_{t_F} = u_{T_{\text{solidus}}} / \dot{T} \quad (14)$$

Temperature uncertainties,  $u_{T_{\text{solidus}}}$  and  $u_{T_{\text{low}}}$ , are calculated using Eq. 6. To execute these calculations, Eq. 1 is first used to find  $S_{\text{solidus}} = \epsilon_{\text{solidus}} * F(1290^\circ\text{C})$  and  $S_{\text{low}} = \epsilon_{\text{solidus}} * F(1000^\circ\text{C})$ , these values are then substituted for  $S$  in Eq. 12, and  $\epsilon_{\text{solidus}}$  is substituted for  $\epsilon$ . The calculation of  $u_{T_{\text{low}}}$  requires the assumption that emissivity at that temperature is equal to  $\epsilon_{\text{solidus}}$ . This assumption is valid based on the work published by Makino et al. [30]. This work demonstrated that for pure nickel, the

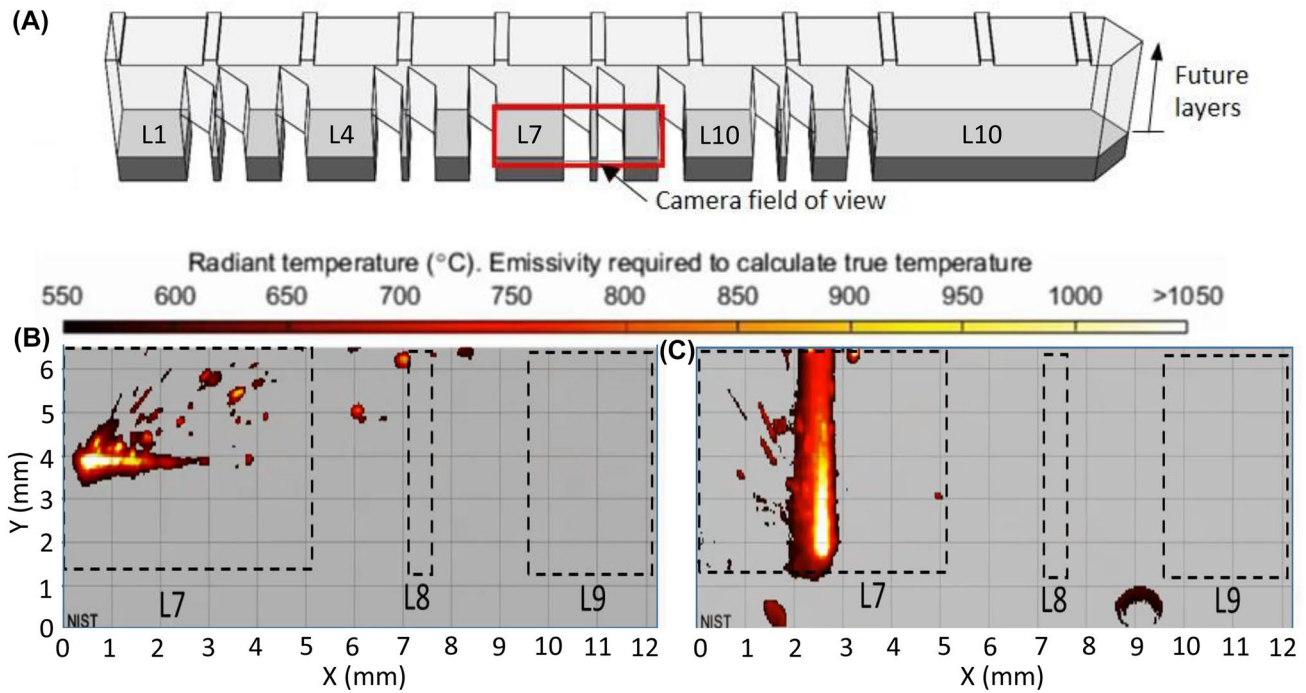


**Fig. 10** Example frames acquired using the high-speed infrared camera. **a** Illustration of the part and camera field of view, **b** Layer 125, –X scan direction, **c** Layer 126, –Y scan direction

temperature dependency of emissivity becomes less significant at shorter wavelengths. Considering the temperature range over which the cooling rate is being measured in the current work (290 °C) and the wavelengths used in this study, which are lower than the minimum investigated by Makino et al. (2 μm), the emissivity is expected to vary by 0.01 or less.

Cooling rate,  $\dot{T}$  (°C/s), is calculated using the temporal approach:

$$\dot{T} = \frac{\Delta T_{\text{true}}}{\Delta t} = \frac{T_{\text{solidus}} - T_{\text{low}}}{t_F - t_{\text{low}}} \quad (15)$$

where  $\Delta T$  is the temperature, in °C, over which the cooling rate is calculated, and  $t_{\text{low}}$  is the time, in s, that the temperature first crosses a pre-defined lower limit after it freezes. The temperature range for cooling rate is arbitrarily chosen to be from the true solidification temperature,  $T_{\text{solidus}} = 1290$  °C, to a lower true temperature of  $T_{\text{low}} = 1000$  °C. The value of  $t_{\text{low}}$  is determined using linear interpolation.

Cooling rate uncertainty,  $u_{\dot{T}}$ , is:

$$u_{\dot{T}}^2 = \left( \frac{\partial \dot{T}}{\partial T_{\text{solidus}}} \right)^2 u_{T_{\text{solidus}}}^2 + \left( \frac{\partial \dot{T}}{\partial T_{\text{low}}} \right)^2 u_{T_{\text{low}}}^2 + \left( \frac{\partial \dot{T}}{\partial \Delta t} \right)^2 u_{\Delta t}^2$$

$$u_{\dot{T}}^2 = \left( \frac{1}{\Delta t} \right)^2 \left( u_{T_{\text{solidus}}}^2 + u_{T_{\text{low}}}^2 \right) + \left( \frac{\Delta T}{\Delta t^2} \right)^2 u_{\Delta t}^2 \quad (16)$$

where  $u_{T_{\text{solidus}}}$  and  $u_{T_{\text{low}}}$  are the uncertainties of  $T_{\text{solidus}}$  and  $T_{\text{low}}$ , and  $u_{\Delta t}$  is the uncertainty of  $t_F - t_{\text{low}}$ , and is considered to be negligible.  $T_{\text{solidus}}$  and  $T_{\text{low}}$  are calculated using Eq. 6.

## Results and Discussion

Figure 10 presents two example frames acquired by the infrared camera. An illustration of the part with the camera field of view highlighted at the completed build height is shown at the top of the figure. Figure 10b shows a frame acquired during Layer 125 as the laser scans from the right to the left across L7. A significant amount of ejecta trails the melt-pool. Figure 10c presents an image acquired during Layer 126. In this frame, the laser scans downward across L7. Each frame only displays the radiant temperature within the measurable range of the camera system.

Although each frame shown in Fig. 10 was acquired as the laser finishes creating the scan-track bisecting L7, the radiant temperature of the two layers appears to be significantly different. The Y direction scan strategy used in the even layer shown in Fig. 10c results in a much larger area detectable by the camera. This area extends from one side of the leg to the other and covers several preceding scan-tracks, totaling an area of approximately 5 mm<sup>2</sup>. In contrast, Fig. 10b shows that the scan-track created while traveling

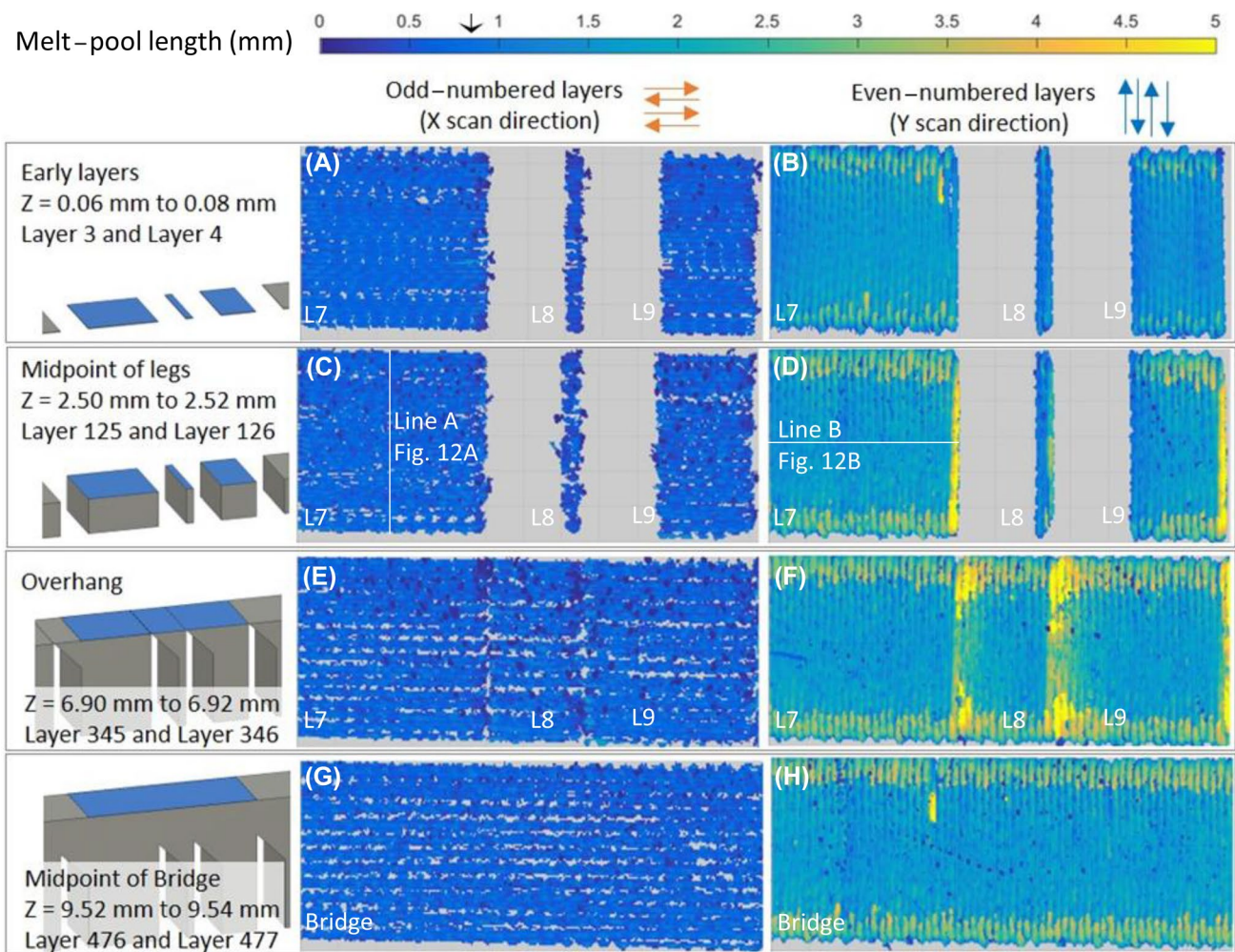


**Fig. 11** The melt-pool length measured at several layers of interest. The field of view of each plot is 12 mm wide and 5 mm tall. The left column illustrates the state of the part in each layer, with the blue highlighted region showing the field of view in the plots. The arrow

on the color bar indicates the single-track melt-pool length reported by Lane et al. [18]. The radiant temperatures along the vertical and horizontal lines in Figure C and D are shown in Fig. 12

in the  $-X$  direction during Layer 125 creates a detectable area that extends half-way across the leg and does not significantly spread perpendicular to the track. This covers an area of approximately  $0.5 \text{ mm}^2$  and is a fraction of the area created in Layer 126 shown in Fig. 10c. This difference suggests that Layer 126 experiences longer melt-pools and slower cooling rates.

### Melt-Pool Length

Figures 11 and 12 confirm longer melt-pools during the even-numbered layers compared to the odd-numbered layers. Figure 11 presents a heat-map of the melt-pool length measured in the field of view during select deposition layers. The colors, ranging from blue to yellow, indicate melt-pool lengths from 0 to 5 mm. The center column (Figures A, C, E, and G) shows odd-numbered layers during which the laser

scans parallel to the  $X$  axis, while the right column (Figures B, D, F, and H) presents even-numbered layers during which the laser scans parallel to the  $Y$  axis. The odd-numbered layers in Fig. 11 are dominated by much darker blue colors, whereas the even-numbered layers are shades of brighter blues, greens, and even yellows. Figure 12 shows the length measurements extracted from the pixels along the lines depicted in Fig. 11c, d and compares them to the single-track scans reported by Lane et al. [18], which are indicated by the horizontal red lines. Please note the different vertical axis scales in the two plots. These plots confirm the observations made of Fig. 11. The melt-pools in L7 during Layer 125 are shorter, typically between 0.5 and 1.0 mm and comparable to the single-track scans. In contrast, the lengths in L7 during Layer 126 are significantly longer, typically between 1 mm and 2 mm and approaching 4–5 mm near the right edge of each feature.

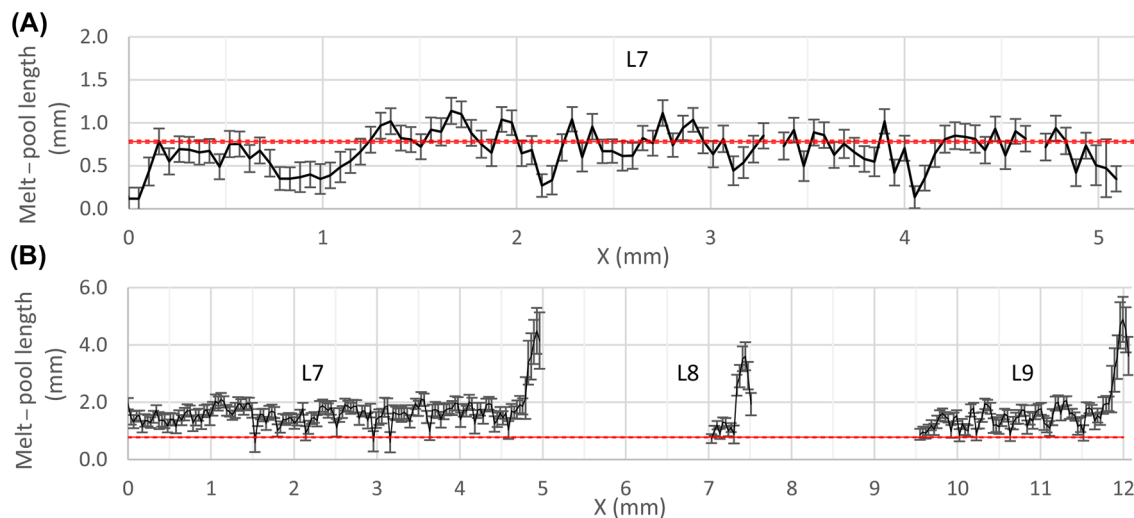


**Fig. 12** Distribution of the melt-pool lengths measured in **a** Layer 125, **b** Layer 126. The red horizontal lines indicate the melt-pool length of single-track scans reported by Lane et al. [18]. Error bars represent the length measurement uncertainty,  $u_L$ , with a coverage of  $1\sigma$

The longer melt-pools in the even-numbered layers result from the limited time between reheat cycles, which keeps the material at elevated temperatures and is less capable of evacuating heat from the melt-pool. For instance, according to the scan strategy details presented in Fig. 5, the material in even-numbered layers is allowed 0.48–13 ms to cool before it is reheated by the adjacent scan-track, as demonstrated in Fig. 9. This results in the melt-pool remaining molten for a longer period of time and appearing to be longer. In contrast, during the odd-numbered scans, which are depicted in Fig. 4, the material cools for 30.1–54.1 ms before the next adjacent scan-track. Thus, the material reaches a lower temperature before being reheated and is more effective evacuating heat from the melt-pool.

The melt-pool length calculation in this work is fundamentally different than the spatial measurements performed in other studies; therefore, caution is required when interpreting the results. Equation 7 defines the melt-pool length in the current work as the duration the material remains molten scaled by the scan speed. This measurement is performed for each individual pixel by considering the change in temperature over time (multiple camera frames). In contrast, other studies of scan-tracks executed on bare surfaces measure the geometric distance from the front of the solidus isotherm to the back [17, 25]. This measurement is performed across pixels in a single instance in time (a single frame).

The geometric method to calculate melt-pool length is not implemented in this work for several reasons. First, the greater variability in surface texture on each layer of the 3D build, compared to bare substrates, results in significant variation in surface emissivity, as demonstrated by Heigel et al. [28]. Since the emissivity cannot be measured over the surface during the process, the radiant temperature isotherms

are irregular, and thus, the geometric measurement could lead to errors. The effect of a layer of consolidated powder on the melt-pool length can be seen in the analysis presented in [25]. The second reason is the difference in time and position of the measurement relative to the laser. In typical geometric measurements, the melt pool length is often regarded as the distance from the front of the melt pool or laser to the tail-end of the melt pool. In contrast, the temporal based measurement described in Eq. 4 describes how far the laser travels ahead before the measurement point solidifies. This distinction is trivial for steady-state scan-tracks when the laser does not change direction; however, it is significant when the laser changes direction, such as the case in the even-numbered layers. The third and final reason is the transient melt-pool that is created when the laser changes direction in even-numbered layers, as depicted in Fig. 5. This results in an atypical melt-pool shape as one scan-track ends and the next begins. Consequently, the “length” of this transient melt-pool cannot be directly compared to the teardrop melt-pool shape that occurs during steady state during welding and AM single scan-tracks. While comparison between odd-numbered layers and single-track scans is appropriate since the laser does not immediately turn around and creates a transient scan-track within the camera field of view, as shown in Fig. 4, comparison with the even-numbered layers is inappropriate since the melt-pool is often transient and is less likely to reach a steady-state condition comparable to single scan-tracks.

### Cooling Rate

Figure 13 shows the cooling rate measured in the layers presented and compared in Fig. 11. Again, a clear difference

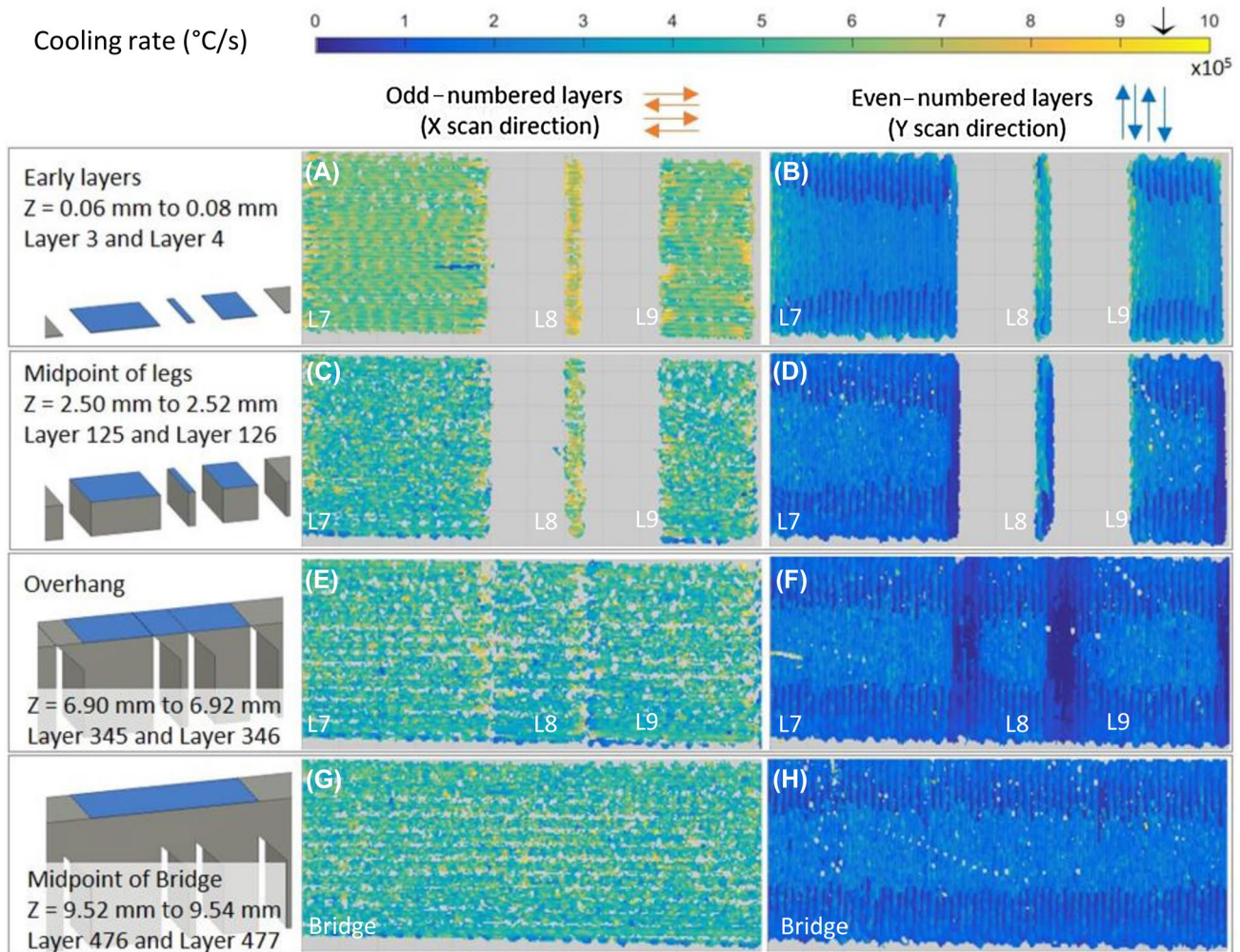


**Fig. 13** The cooling rate measured at several layers of interest. The field of view of each plot is 12 mm wide and 5 mm tall. The left column illustrates the state of the part in each layer, with the blue high-

lighted region showing the field of view in the plots. The arrow on the color bar indicates the single-track melt-pool length reported by Lane et al. [18]

exists in the cooling rate between the even- and odd-numbered layers. However, the trend is opposite to the melt-pool length: Even-numbered layers have lower cooling rates and longer melt-pools, while odd-numbered layers have faster cooling rates and shorter melt-pools. The inverse relationship between melt-pool length and cooling rate is well known in the welding and AM communities. As expected, the cooling rate is comparatively lower in locations where the feature geometry restricts the flow of heat from the melt-pool. For instance, lower cooling rates are evident along the right side of each feature and along the left edge of the overhangs. These regions also exhibited significantly longer melt-pools (Fig. 11).

A quantitative analysis of the cooling rate is necessary to explore the impact of scan strategy and feature geometry, to provide context for the accompanying post-process measurements, and to provide validation data for process models.

Figure 14 displays histogram plots of each of the layers presented for analysis. The individual features being created in these layers are differentiated to facilitate comparison. Table 2 provides the number of samples (pixels) in each histogram and the calculated mean, median, and standard deviation. This table is arranged according to the size of each feature in descending order.

The histograms presented in Fig. 14 are Gaussian in character with two exceptions: 1) the small leg, and 2) the secondary peak around  $0.5 \times 10^5$  °C/s in the even-numbered layer. The small leg does not exhibit a Gaussian distribution in any of the three even-numbered layers. This may be caused by a variety of factors: first, the limited number of pixels available for sampling due to the small size of the leg and the few scan-tracks required in each layer. Second, the small leg does not reach a “steady-state” condition. The temperature of a leg increases as the scan-tracks advance

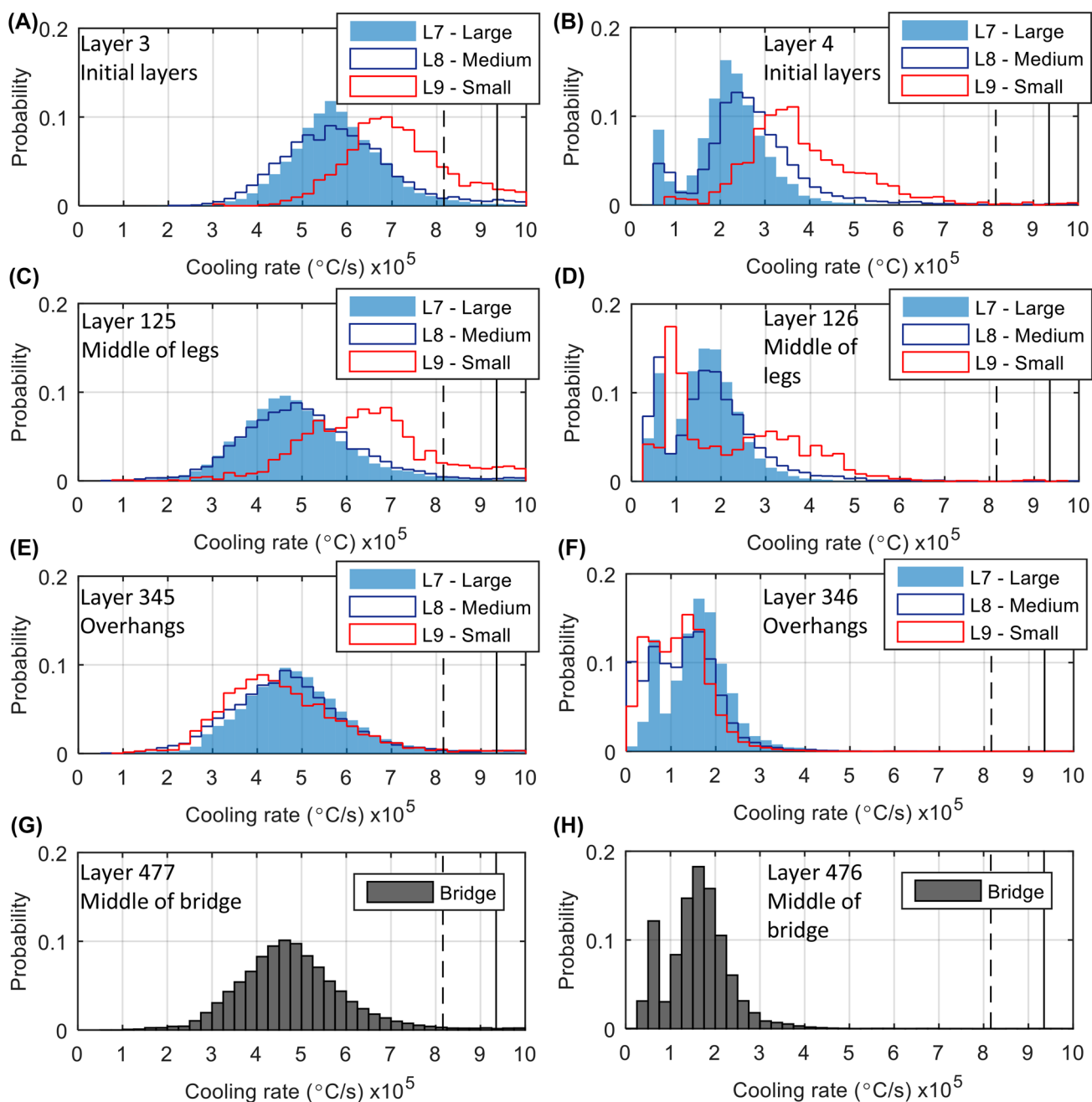


**Fig. 14** The distribution of cooling rate measurements in each feature during the layers presented in Fig. 13

across the leg. Consequently, the cooling rate progressively decreases as the leg becomes less capable of absorbing the heat from each successive scan-track. While the other legs and bridge reach a “steady-state” condition, this is not achieved in the small leg. Third, the final scan-track, located along the right edge of each leg where less heat can be evacuated, accounts for a larger percentage of the number of pixels being analyzed in the small leg compared to the other features.

The secondary peak in histograms of the even-numbered layers is a consequence of the cooling rate calculation methodology. Figure 15 presents the radiant temperature extracted across three horizontal lines bisecting the large leg (L7) in Layer 126. Each line in Fig. 15 exhibits cooling rates that fluctuate from approximately  $0.5 \times 10^5$  to  $3.0 \times 10^5$  °C/s, though the nature of this fluctuation depends on the location of the bisecting line. The cooling rates in Line B are near  $0.5 \times 10^5$  °C/s within 0.2 mm of the right-most edge, but are otherwise between  $1 \times 10^5$  and  $3 \times 10^5$  °C/s with no

**Table 2** Summary of the cooling rate measurements presented in the histograms in Fig. 14

Feature	Layer	Odd-numbered layers				Even-numbered layers			
		<i>n</i>	Mean (°C/s)	Median (°C/s)	SD (°C/s)	<i>n</i>	Mean (°C/s)	Median (°C/s)	SD (°C/s)
Bridge	476 and 477	30,329	4.79E+5	4.70E+5	1.81E+5	36,305	1.62E+5	1.62E+5	8.66E+4
L7 (large) (5×5) mm	3 and 4	12,919	5.78E+5	5.71E+5	1.76E+5	14,699	2.21E+5	2.22E+5	1.01E+5
	125 and 126	13,044	4.83E+5	4.72E+5	1.72E+5	15,002	1.67E+5	1.67E+5	8.90E+4
	345 and 346	12,270	4.88E+5	4.78E+5	1.74E+5	14,950	1.62E+5	1.62E+5	8.98E+4
L9 (medium) (2.5×5) mm	3 and 4	6407	5.80E+5	5.71E+5	1.91E+5	7491	2.69E+5	2.57E+5	1.31E+5
	125 and 126	6404	4.98E+5	4.88E+5	1.90E+5	7598	1.80E+5	1.72E+5	1.16E+5
	345 and 346	11,358	4.69E+5	4.62E+5	1.93E+5	14,213	1.25E+5	1.27E+5	9.07E+4
L8 (small) (0.5×5) mm	3 and 4	1031	7.10E+5	6.99E+5	1.82E+5	1305	3.85E+5	3.61E+5	1.40E+5
	125 and 126	1100	6.40E+5	6.37E+5	1.90E+5	1378	2.23E+5	1.84E+5	1.57E+5
	345 and 346	5802	4.58E+5	4.39E+5	1.88E+5	7529	1.16E+5	1.15E+5	8.09E+4

The reported standard deviation is the root sum square of the average measurement uncertainty,  $u_T$ , the standard deviation of cooling rates measured in all pixels in each feature. Note that the large standard deviations are primarily a result of the measured variability within each feature

significant pattern. In contrast, the cooling rates along Lines A and C show a regular oscillation with a minimum value of  $0.5 \times 10^5$  °C/s and a period approximately equal to twice the hatch spacing (0.2 mm), suggesting the effect is a result of the scan pattern. Along both of these lines, as in the case of Line A, the cooling rate is consistently lower (around  $0.5 \times 10^5$  °C/s) at the right-most edge.

Figure 16 facilitates close inspection of the radiant temperature history of the six points highlighted in Fig. 15 and proves that the peaks at low cooling rates are an artifact of the methodology. The time scales in these plots have been shifted so the creation of the melt-pool occurs at 0 s. The left plot shows the temperature history from points near the middle of the part. Point B' decreases in radiant temperature in a consistent manner until it reaches approximately 660 °C, at which point it is reheated by the next laser pass. During this rapid decrease in temperature, the calculated cooling rate is  $1.6 \times 10^4$  °C/s. In contrast, as Points A' and C' cool, they are reheated sooner by the next laser pass, prolonging their time above the lower radiant temperature threshold used to calculate the cooling rate, resulting in cooling rates approximately equal to  $0.6 \times 10^4$  °C/s. However, if only the slope of curve is considered before it is reheated, the cooling rate of all three points in Fig. 16a appears to be equivalent. This confirms that the lower cooling rate measured near the top and bottom edges is an artifact of the calculation method. This does not mean that the reported values are not of interest, since they directly reflect real conditions occurring in these parts of the sample. Instead, it suggests that care must be taken when defining cooling rates for analysis and comparing results between studies.

Not all of the low cooling rate values in the even-numbered layers are a function of the calculation methodology. The low cooling rate measured at the right edge where the final scan-track occurs is not an artifact and is a result of the

feature geometry. Figure 16b shows that the pixels measuring material in the final scan-track solidify then cool in a consistent manner, with no temperature increases due to subsequent laser passes. These slopes are visibly shallower than the slopes presented in Fig. 16a and confirm that the material does in fact cool at a slower rate. This occurs because the material solidified by the final scan-track in each feature is partially surrounded by powder, which acts as an insulator and inhibits cooling.

A comparison of the cooling rates in each of the four features suggests that the large leg (L7) can serve as a proxy for the material in the bridge. A comparison of L7 in Layers 125 and 126 to the bridge in Layers 476 and 477 shows little difference between the histogram shapes (Fig. 14c vs. g and Fig. 14d vs. h). In fact, the mean, and median values reported in Table 2 differ by no more than 5000 °C/s, which is less than 1% in the odd-numbered layers and approximately 3% in the even-numbered layers. The medium size leg is also similar to the large leg, 3% higher in Layer 125 and 8% and 3% higher in mean and median (respectively) in Layer 126. The differences between the small and large legs are even greater. During Layer 125, the mean and median cooling rates of the small leg are 33% and 35% faster, and during Layer 126, the mean and median cooling rates are 38% and 19% faster. These results suggest that the large leg, which is cross-sectioned and analyzed by Stoudt et al. [20] and Zhang et al. [21], can serve as a proxy for the bridge, and possibly the medium sized leg. However, the small leg, which is also cross-sectioned by Stoudt et al., warrants separate consideration.

Figure 17 shows the median cooling rate measured in each feature of every frame in IN 625 Builds 1 and 2. This figure reinforces that the selected layers presented for analysis in the earlier figures (Layers 3, 4, 125, 126, 345, 346, 476, and 477) are representative of both builds. The



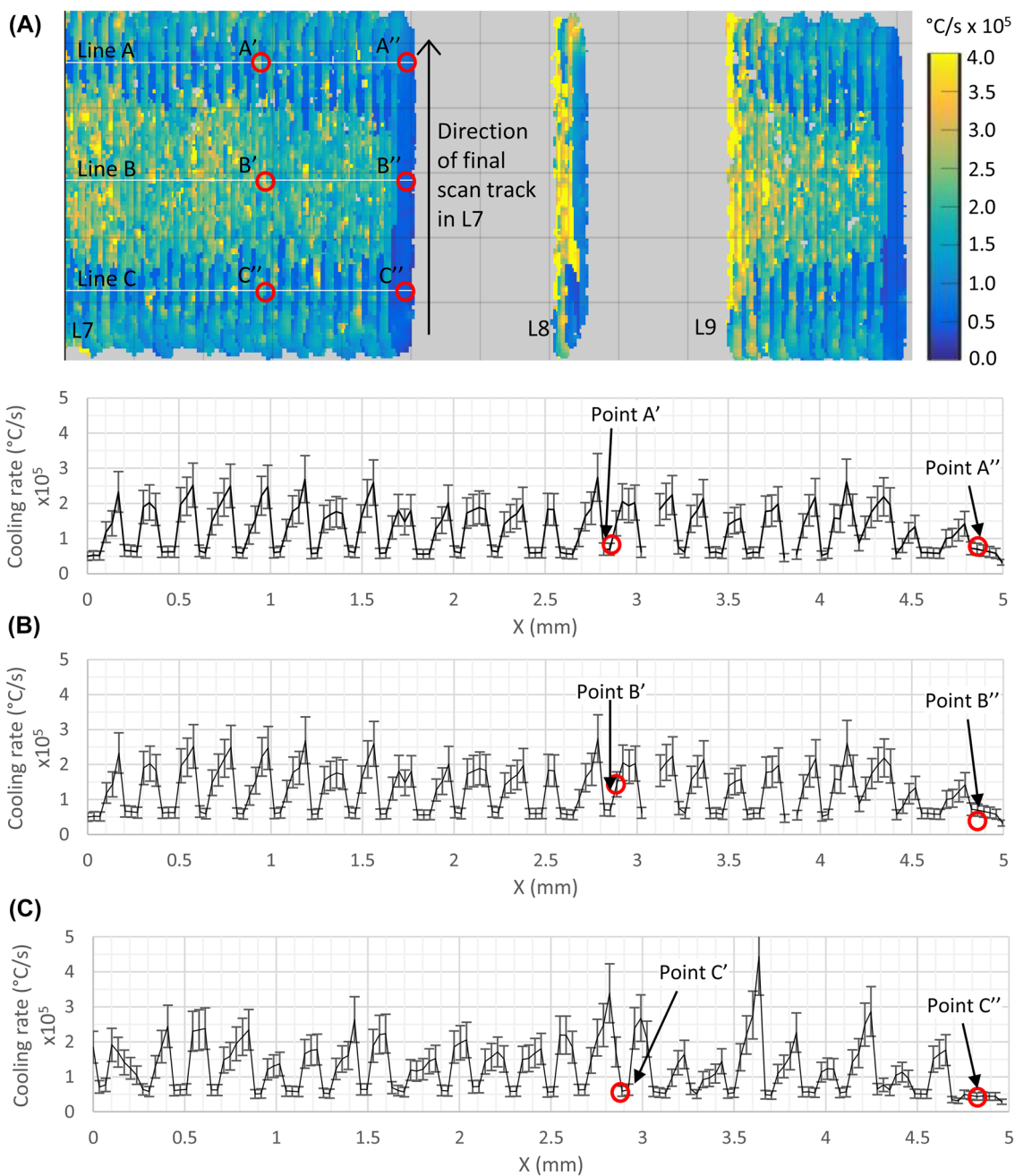


**Fig. 15** The measured cooling rate along several lines crossing Leg 7. The top illustration shows the cooling rate measurements shown first in Fig. 11 and the approximate location of the analysis lines. **a–c** The radiant cooling rate of every pixel along the three lines in L7. The

temperature profiles of the highlighted points are shown in Fig. 16. Error bars represent the cooling rate measurement uncertainty,  $u_T$ , with a coverage of  $1\sigma$

inconsistent measurement of the small leg (L9) is likely a function of the relatively few pixels used for analysis, as discussed earlier, and the fluctuations should not be interpreted as inconsistencies in the build process. The vertical line in each plot located at layer 50 and labeled “A” marks the transition into steady state, where the difference between layers become negligible. This suggests that material deposited

1 mm above the substrate is consistent and should be used for post-process analysis. The higher cooling rates in the early layers that are in close proximity of the substrate, which acts as a heat-sink, are also evident in Fig. 13 and the histograms in Fig. 14. The transition to steady state in the bridge after the completion of the overhangs occurs sooner, after approximately 20 layers, or 0.4 mm.

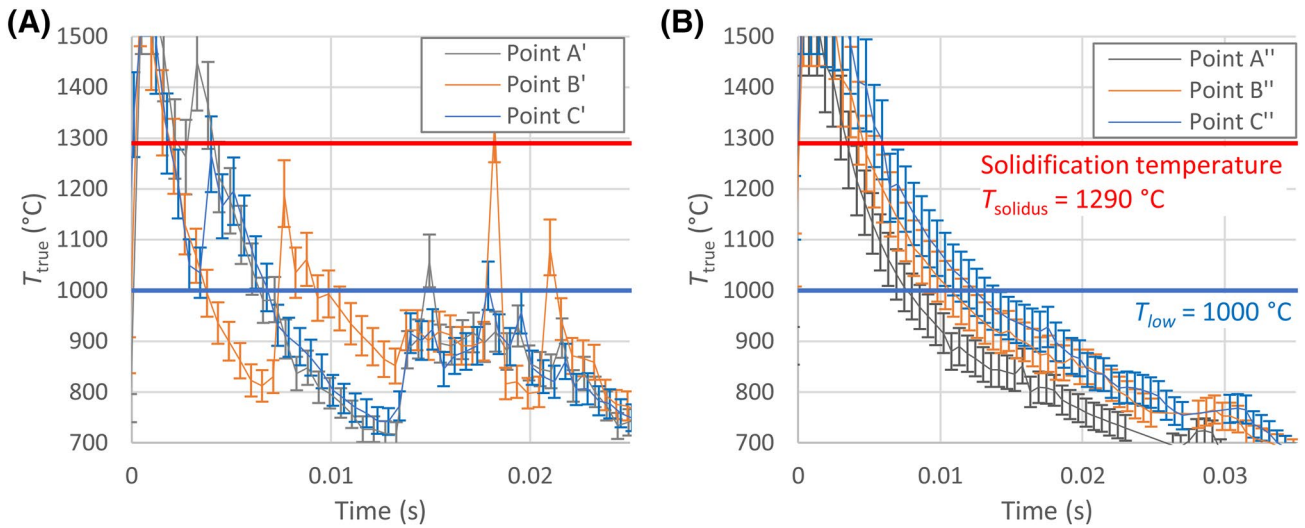


**Fig. 16** Temperature profiles of select pixels in Layer 126. The location of pixels is shown in Fig. 15. **a** Pixels along Lines A, B, and C nearer the middle of L7, **b** pixels along the same line extracted near

the edge of L7. Error bars represent the RMSE of the thermal camera calibration. Error bars represent the true temperature measurement uncertainty,  $u_{T_{true}}$ , with a coverage of  $1\sigma$

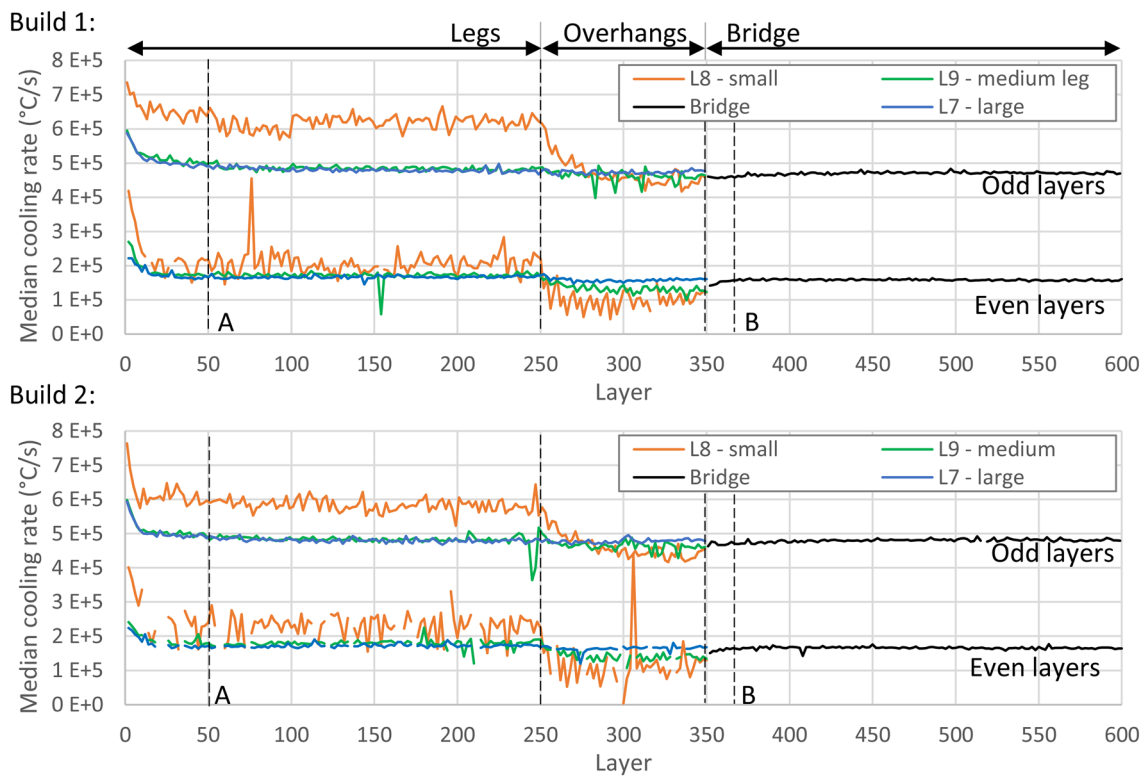


**Fig. 17** The median cooling rate measured in each feature for the entirety of Builds 1 and 2. The vertical line labeled “A” denotes the transition to steady state. The line labeled “B” denotes the transition to steady state in the bridge

## Conclusions

This work presented in situ temperature measurements acquired using high-speed IR thermography to measure melt-pool lengths and cooling rates at every layer during multiple 3D builds, and thermocouples to measure the temperature of the substrate and build volume. Thermography was performed using a high-speed IR camera (frame rate of 1800 Hz and an integration time of 40  $\mu$ s) observing an area approximately 12 mm long and 6 mm wide.

The results presented in this study provide valuable data for thermal model validation, offer context for the post-process residual stress, distortion, and microstructure analysis, and reveal how appropriate single-track experiments are for studying complex 3D builds. However, care must be taken in interpreting these results and applying them to other studies due to the measurement limitations and methodology. For instance, the thermal camera used in this study is limited to radiant temperatures between 550 and approximately 1100 °C. Much of the part surface in each layer is below this temperature range just as much of the melt-pool is at a higher temperature and saturates the camera. Furthermore, the spatial and temporal resolution of the camera (pixel iFOV of approximately 52  $\mu$ m  $\times$  34  $\mu$ m, frame rate of 1800 Hz) limits the measurements that can be made, such as melt-pool width, and more-than-likely adversely affects the measurement uncertainty beyond the initial estimates made in this work. Further work is required to define this uncertainty and will be reported in a future publication. In the meantime, when comparing to thermal models, the predictions must be processed in a manner that makes an adequate comparison. Both cooling rate and melt-pool length must be calculated in the same way to capture the same phenomena, such as the longer cooling rates observed in the even layers due to reheating within the temperature band used to calculate cooling rate.

Regarding the significance of the results reported herein, as they related to accompanying post-process measurements reported in this issue [19–21], both cooling rate and melt-pool length comparisons between the four features (large leg, medium leg, small leg, and bridge) show that the large leg, which measures 5 mm  $\times$  5 mm, has a similar thermal history to the medium sized leg and the bridge. This suggests that the microstructure created in the large leg is the same as in the bridge and conceivably 5 mm  $\times$  5 mm cubes can serve as witness artifacts for larger features, though further work is required to prove this hypothesis. This may depend on the scan strategy and material.

Although the 5-mm square legs exhibit similar thermal histories to larger features, they are not appropriate proxies for much thinner features. The small legs in this study,

which are 1/10th the size (measuring 0.5 mm  $\times$  5 mm), experience cooling rates that are notably faster. It is reasonable to assume that this will lead to different material states, though this conclusion requires further investigation. Fortunately, Stoudt et al. [20] and Zhang et al. [21] provide comparisons of cross sections obtained by the large and small legs in this study.

The greatest difference in cooling rate and melt-pool length is caused by the atypical scan strategy used in this study, in which the time between adjacent scan-tracks varies greatly. The intent of the scan strategy was for simplicity in model implementation and to avoid overlaps of scan corridors, which could cause voids and vary the thermal history. Unfortunately, the scan strategy resulted in vast differences in the time between adjacent scans (0.48–13 ms for even layers and 34–54 ms for odd layers in the legs) which greatly impacted the melt-pool length and cooling rates. At this time, it is unclear if the differences in layers will cause discernible difference in the post-process results. It is possible that the longer melt-pools in the even-numbered layers also create deeper melt-pools and the associated thermal impact penetrates deeper than the odd layers. If so, the thermal histories of the even layers would be the dominate effect. However, further work is required to study this implication.

The melt-pool and cooling rate measurements reported in this study do not compare well to those of single-track scans on bare plates. While the odd-layer melt-pool length measurements are similar to those reported by Lane et al. [18] for single tracks using the same machine, alloy, power, and scan speed, the cooling rate is much slower. This suggests that either the relationships between melt-pool length and cooling rate for single-track scans are not relevant for 3D builds or information extracted from the single-track scans on bare plates, such as solidification radiant temperature and emissivity, cannot be implemented for measurements on 3D builds. Further work is required to understand this difference.

Finally, both the melt-pool length and cooling rate of the even-numbered layers are significantly different than single-track scans. For instance, during steady state in the bulk of the large leg, the melt-pool length in the even layers is twice as long and the cooling rate is approximately five times smaller. In the extreme instances of the final scan-track at the edge of the part, the melt-pool length is nearly 5 times longer and the cooling rate is an order of magnitude smaller. These results suggest that while single-track scans can be used as a tool for preliminary process-parameter mapping [26, 27], caution must be exercised when relating microstructural analyses of single-tracks to the 3D build.

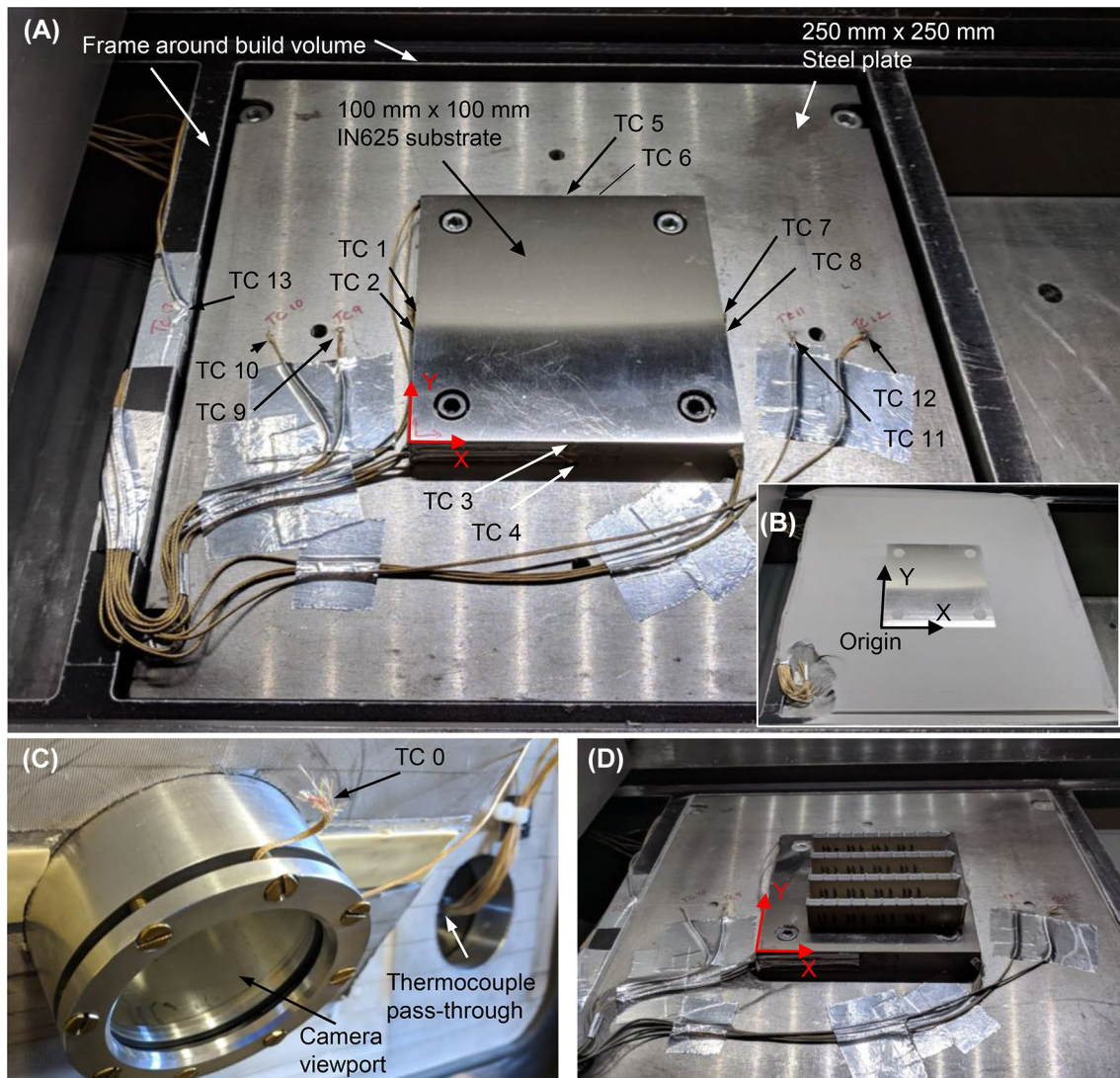


**Fig. 18** The thermocouple measurement setup. **a** Location of 12 of 13 thermocouples in the build volume. **b** Powder packed around the IN625 substrate shortly before the build begins. **c** The viewport on

the door with TC 0 and the wire pass-through. **d** The completed build with powder removed

**Table 3** Locations of each thermocouple relative to the substrate origin

	TC 1	TC 2	TC 3	TC 4	TC 5	TC 6	TC 7	TC 8	TC 9	TC 10	TC 11	TC 12	TC 13 <sup>a</sup>
X (mm)	0	0	50	50	50	50	100	100	-25	-50	175	200	-75
Y (mm)	50	50	0	0	100	100	50	50	50	50	50	50	50
Z (mm)	0	-6.35	0	-6.35	0	-6.35	0	-6.35	-6.35	-6.35	-6.35	-6.35	-4 (start), 8.5 (end)

<sup>a</sup>The Z location of TC 13 varies during the build because the substrate increments down with each layer

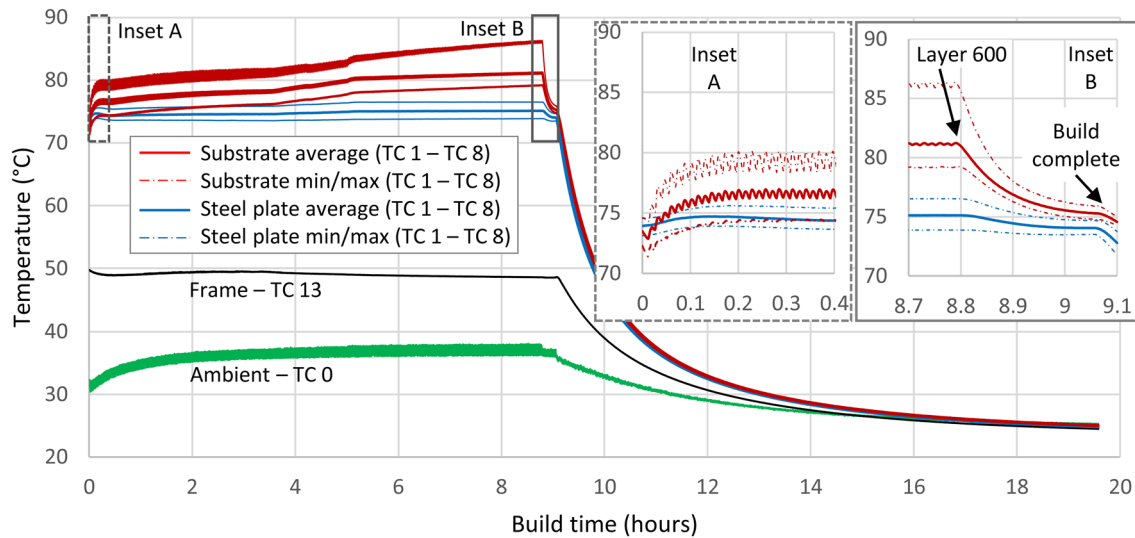


**Fig. 19** Overview of the thermocouple measurements. TC 1 through TC 8 are shown in greater detail in Fig. 20

## Compliance with Ethical Standards

**Conflict of interest** On behalf of all authors, the corresponding author states that there is no conflict of interest.

## Appendix

### Thermocouple Measurement Method

An additional IN625 build was performed several months after the original AM-Bench experiments with thermocouples located at various locations on the substrate and in the build chamber. This additional build was performed to provide greater insight into the temperature at locations on the substrate and build volume to enable modelers to adequately define the boundary conditions. Note that these thermocouple measurements were not available at the time of the AM-Bench competition. The only differences between this build and the earlier builds are that the laser was replaced and calibrated by the manufacturer, and the build completed 16 min sooner.

A total of 14 thermocouples were included in the build volume, as depicted in Fig. 18. Each thermocouple (Omega GG-K-30 type K) has a measurement uncertainty equal to the larger of 2.2 °C or 0.75%. The signals are acquired using a National Instruments NI 9213 module at a rate of 1 Hz. The thermocouple wires are welded to the steel plate and IN625 substrate using a spot welder. Each wire is stress-relieved using aluminum tape, which is evident in the images in Fig. 18.

Table 3 presents the approximate locations of each thermocouple (excluding TC 0) relative to the top front left corner of the IN625 substrate. One thermocouple (labeled TC 0) is attached to the custom door and hangs just above the viewport. This thermocouple is used to measure the temperature of the build chamber environment. Eight thermocouples (TC 1 through TC 8) are welded to the upper and lower edges of the sides of the IN625 substrate. The thermocouples were welded to the top and bottom edges at the mid-point of each side. This placement prevented the thermocouples from interfering with the recoating blade or the larger (250 mm by 250 mm) steel build plate on which the IN625 substrate is bolted. Four thermocouples (TC 9 through TC 12) are welded to the steel build plate, on a line parallel to the X axis that bisects the IN625 substrate. TC 13 is adhered to the frame around the build volume using aluminum tape. This thermocouple, along with those welded to the build plate (TC 9 through TC 12) and those welded to the left and right sides of the substrate (TC 1, 2, 7, and 8), is coplanar.

### Substrate Temperature Results

Figure 19 presents an overview of the measurements acquired by all thermocouples. When the build begins, the ambient gas in the build chamber is approximately 32 °C, the frame around the build volume is 49.8 °C, the steel plate is on average 73.9 °C (four thermocouples measuring between 73.1 and 74.5 °C), and the IN625 substrate is on average 73.5 °C (eight thermocouples measuring between 72.2 and 74.6 °C). Although the build plate temperature was set to 80 °C for the build, the steel plate never reached

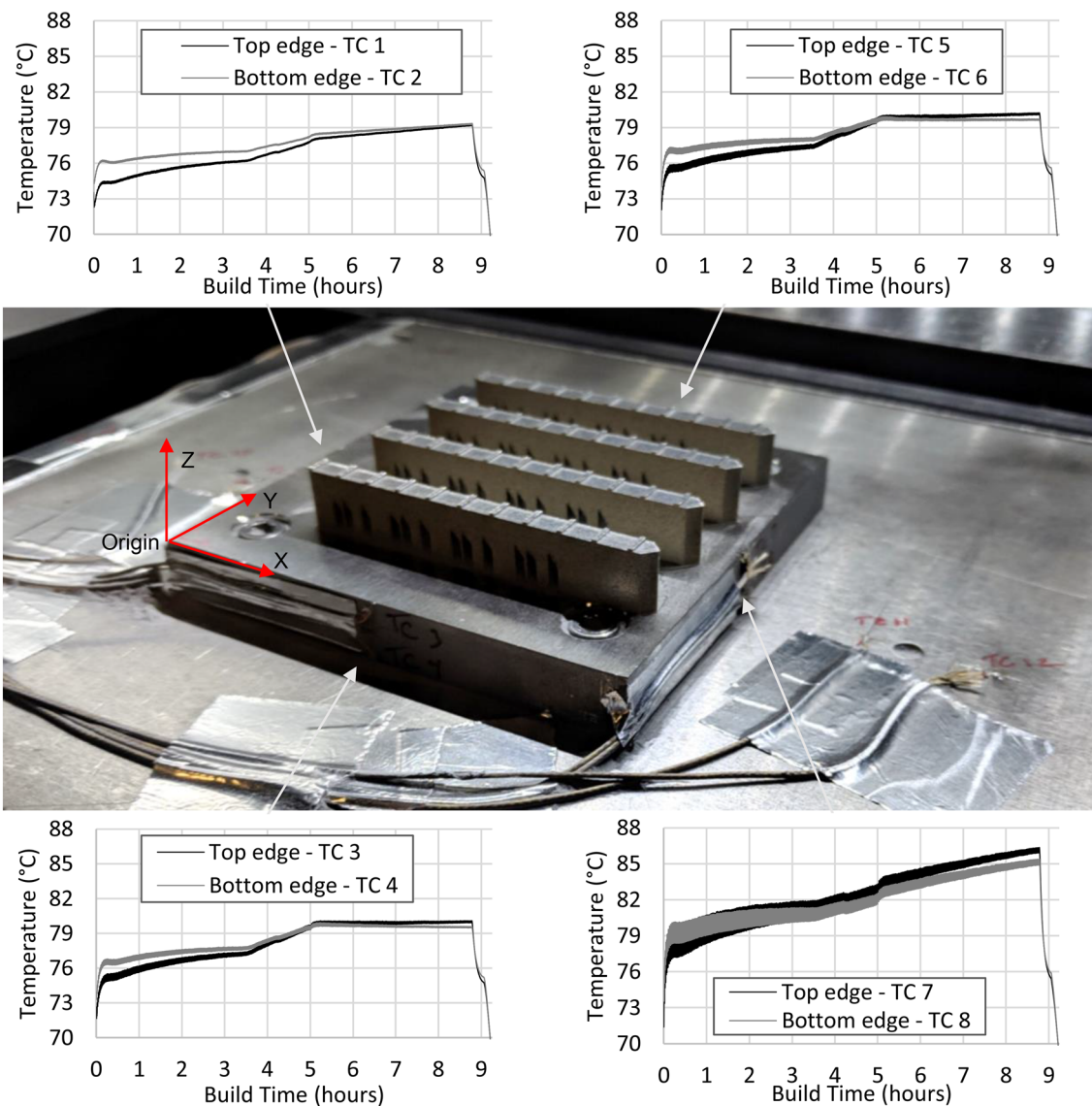


**Fig. 20** Measurements from thermocouple welded to the IN625 substrate

this temperature, and it was not until after the build started and the laser began providing heat to the substrate did a portion of it reach 80 °C. In fact, a majority of the thermocouples remained below the programmed build plate temperature. During the build, the ambient thermocouple (TC 0) increased to a maximum of 38 °C during the build, while the thermocouple attached to the frame around the build volume actually decreased slightly in temperature during the build to 48.5 °C. This decrease in temperature is likely due to the fact that as the build progresses, and the part grows in height, the build platform lowers, thus increasing the distance between it and the location of TC 13.

Figure 20 presents the temperature history measured by the thermocouples welded to the IN625 substrate (TC

1 through TC 8). The greater temperature increases occur on the right side (positive  $X$ ) of the substrate. This likely occurs because the bridge artifacts are positioned closer to this side than any other. There is a clear inflection point at the transitions between the legs and overhangs (Layer 350 at approximately 3.5 h) and between the overhangs and the bridge (Layer 450 at approximately 5 h). During the deposition of the overhang, it appears the temperature increases more rapidly for thermocouples TC 1 through TC 6. Once the bridge begins to build around the fifth hour, the temperature increase is much more gradual and practically reaches a steady state in some instances.

## References

- Denlinger ER, Michaleris P (2017) Mitigation of distortion in large additive manufacturing parts. *Proc Inst Mech Eng Part B J Eng Manuf* 231(6):983–993
- Denlinger ER, Heigel JC, Michaleris P (2014) Residual stress and distortion modeling of electron beam direct manufacturing Ti–6Al–4V. *Proc Inst Mech Eng Part B J Eng Manuf* 229:0954405414539494
- Dunbar AJ, Denlinger ER, Gouge MF, Michaleris P (2016) Experimental validation of finite element modeling for laser powder bed fusion deformation. *Addit Manuf* 12:108–120
- Bagg SD, Sochalski-Kolbus LM, Bunn JR (2016) The effect of laser scan strategy on distortion and residual stresses of arches made with selective laser melting. In: *ASPE/euspen 2016 summer topical meeting on dimensional accuracy and surface finish in additive manufacturing*, June 27–30, 2016, Raleigh, North Carolina, USA. <http://toc.proceedings.com/47967webtoc.pdf>
- Strantz M et al (2018) Coupled experimental and computational study of residual stresses of additively manufactured Ti–6Al–4V components. *Mater Lett* 231:221–224
- David S, Vitek J (1989) Correlation between solidification parameters and weld microstructures. *Int Mater Rev* 34(1):213–245
- Antony AA, Meyer J, Prangnell P (2013) Effect of build geometry on the  $\beta$ -grain structure and texture in additive manufacture of Ti6Al4V by selective electron beam melting. *Mater Charact* 84:153–168
- Dehoff R et al (2015) Site specific control of crystallographic grain orientation through electron beam additive manufacturing. *Mater Sci Technol* 31(8):931–938
- Kriczky DA, Irwin J, Reutzel EW, Michaleris P, Nassar AR, Craig J (2015) 3D spatial reconstruction of thermal characteristics in directed energy deposition through optical thermal imaging. *J Mater Process Technol* 221:172–186
- Carroll BE, Palmer TA, Beese AM (2015) Anisotropic tensile behavior of Ti–6Al–4V components fabricated with directed energy deposition additive manufacturing. *Acta Mater* 87:309–320
- Bennett JL et al (2018) Cooling rate effect on tensile strength of laser deposited Inconel 718. *Procedia Manuf* 26:912–919
- Krauss H, Eschey C, Zaeh M (2012) Thermography for monitoring the selective laser melting process. Presented at the proceedings of the solid freeform fabrication symposium, pp 999–1014
- Craeghs T, Clijsters S, Kruth J-P, Bechmann F, Ebert M-C (2012) Detection of process failures in layerwise laser melting with optical process monitoring. *Phys Proc* 39:753–759
- Heigel JC, Whinton E (2018) Measurement of thermal processing variability in powder bed fusion. In: *2018 ASPE and Euspen summer topical meeting advancing precision in additive manufacturing*, Berkeley, pp 242–274
- Hooper PA (2018) Melt pool temperature and cooling rates in laser powder bed fusion. *Addit Manuf* 22:548–559
- Lane B et al (2016) Thermographic measurements of the commercial laser powder bed fusion process at NIST. *Rapid Prototyp J* 22(5):778–787
- Arısoy YM, Criales LE, Özel T, Lane B, Moylan S, Donmez A (2017) Influence of scan strategy and process parameters on microstructure and its optimization in additively manufactured nickel alloy 625 via laser powder bed fusion. *Int J Adv Manuf Technol* 90(5–8):1393–1417
- Lane B, Heigel J, Ricker R et al (2020) Measurements of melt pool geometry and cooling rates of individual laser traces on IN625 bare plates. *Integr Mater Manuf Innov*. <https://doi.org/10.1007/s40192-020-00169-1>
- Phan T et al (2019) Elastic strain and stress measurements and corresponding part deflections of 3D AM builds of 15-5 and IN625 AM-Bench artifacts using neutron diffraction, synchrotron X-ray diffraction, and mechanical measurements. *Integr Mater Manuf Innov* 8(3):318–334
- Stoudt M, Williams ME, Claggett S, Heigel JC, Levine LE (2019) Location-specific microstructure within 3D AM builds of 15-5 and IN625 AM-Bench artifacts. *Integr Mater Manuf Innov*. <https://doi.org/10.1007/s40192-020-00172-6>
- Zhang F, Levine LE, Allen AJ et al (2019) Phase fraction and evolution of additively manufactured (AM) 15–5 stainless steel and inconel 625 AM-bench artifacts. *Integr Mater Manuf Innov* 8:362. <https://doi.org/10.1007/s40192-019-00148-1>
- Heigel JC, Lane BM, Levine LE, Phan TQ, Whiting J (2019) Thermography of the metal bridge structures fabricated for the 2018 additive manufacturing benchmark test series. *J Res Natl Inst Stand Technol* 125:125005. <https://doi.org/10.6028/jres.125.005>
- Moylan S, Whinton E, Lane B, Slotwinski J (2014) Infrared thermography for laser based powder bed fusion additive manufacturing processes. In: *40th annual review of progress in quantitative nondestructive evaluation AIP conference proceedings*
- Lane B, Whinton E (Dec 2015) Calibration and measurement procedures for a high magnification thermal camera. National Institute of Standards and Technology, Gaithersburg, MD, NISTIR 8098
- Heigel J, Lane B (2017) The effect of powder on cooling rate and melt-pool length measurements using in situ thermographic techniques. In: *Proceedings of the 2017 annual international SFF symposium*
- Montgomery C, Beuth J, Sheridan L, Klinbeil N (2015) Process mapping of Inconel 625 in laser powder bed additive manufacturing. Presented at the solid freeform fabrication symposium, Austin, pp 1195–1204
- Vasinonta A, Beuth JL, Griffith M (2007) Process maps for predicting residual stress and melt-pool size in the laser-based fabrication of thin-walled structures. *J Manuf Sci Eng* 129(1):101–109
- Heigel JC, Lane BL, Moylan SP (2016) Variation of emissivity with powder bed fusion build parameters. Presented at the solid freeform fabrication symposium, Austin, pp 1660–1669
- Taylor BN, Kuyatt CE (1994) Guidelines for evaluating and expressing the uncertainty of NIST measurement results. NIST technical note 1297
- Makino T, Kawasaki H, Kunitomo T (1982) Study of the radiative properties of heat resisting metals and alloys: (1st report, optical constants and emissivities of nickel, cobalt and chromium). *Bull JSME* 25(203):804–811